Physical and optical properties of persistent contrails: Climatology and interpretation

Hironobu Iwabuchi,[1] Ping Yang,[1] K. N. Liou,[2] and Patrick Minnis[3]

Received 17 October 2011; revised 9 February 2012; accepted 12 February 2012; published 29 March 2012.

[1] The physical and optical properties of persistent contrails were studied with the measurements made by the Moderate Resolution Imaging Spectroradiometer (MODIS) and the Cloud-Aerosol Lidar and Infrared Pathfinder Satellite Observations (CALIPSO) lidar. MODIS data were used to determine the contrail locations on the basis of their artificial shapes easily distinguished from natural cirrus, and the so-identified contrails were analyzed with collocated CALIPSO lidar data. Statistics of the geography, geometry, meteorology, and optical properties are reported for approximately 3400 persistent contrails observed over North America, the North Atlantic Ocean, and Europe. The majority of the detected contrails appear in ice-supersaturated air with temperatures lower than −40°C. On average, contrails have significantly larger backscattering coefficients and slightly higher linear depolarization ratios (LDRs) than neighboring cirrus clouds. Depolarization tends to be strong when ice crystals are small, and LDR is approximately 0.4–0.45 for young contrails and contrail cores. The mean LDR for the detected contrails increases with decreasing temperature and is not strongly dependent on the lidar pointing angle. The backscattering properties suggest that contrails are primarily composed of small, randomly oriented ice crystals but may also contain a few horizontally oriented plates. Most contrails are optically thin with a mean (median) optical thickness of approximately 0.19 (0.14); however, optically thicker contrails do exist and tend to occur in warmer and more humid ambient air. The mean value and range of the observed LDR data are consistent with theoretical predictions based on a mixture of nonspherical ice crystals randomly oriented in the atmosphere.

Citation: Iwabuchi, H., P. Yang, K. N. Liou, and P. Minnis (2012), Physical and optical properties of persistent contrails: Climatology and interpretation, *J. Geophys. Res.*, *117*, D06215, doi:10.1029/2011JD017020.

1. Introduction

[2] Contrails formed from aircraft exhaust comprise an important component of aviation's impact on the terrestrial climate system because of perturbations in the radiation budget and hydrological cycle of the Earth-atmosphere system. The annual-mean global coverage of line-shaped contrails is small (about 0.1% for the year 2002); however, regional coverage can be much higher (about 2% in the United States and Europe) over active air traffic areas [*Palikonda et al.*, 2005; *Burkhardt and Kärcher*, 2011]. Contrails can cool the surface during daytime but appear to have an overall net warming effect on the atmosphere-surface system, that is, positive radiative forcing at the top of the atmosphere [*Meerkötter et al.*, 1999]. Persistent, line-shaped contrail global radiative forcing is estimated to be 0.012–0.016 W m^{-2} for the years 1992–2005 with uncertainties in the range of 0.005–0.048 W m^{-2}, but our understanding of these uncertainties has been limited [*Minnis et al.*, 2004; *Lee et al.*, 2009; *Kärcher et al.*, 2010; *Voigt et al.*, 2011]. In the next decades, the regional and global climatic impact of aviation-related emissions is likely to continuously increase at a rapid rate [*Marquart et al.*, 2003]. The largest uncertainties in assessing contrail radiative forcing have been caused by a lack of knowledge of both contrail coverage, and the optical properties, especially optical thickness, of persistent contrails [*Schumann*, 2002; *Kärcher et al.*, 2010].

[3] Persistent contrails can exist for hours and grow into irregularly shaped cirrus-like clouds defined as "contrail cirrus" [*Minnis et al.*, 1998; *Heymsfield et al.*, 2010]. Nonlinear contrail cirrus have been difficult to detect from satellite imagery [*Minnis et al.*, 2005]; however, their radiative forcing as a whole was recently assessed to be about nine times larger than that from line-shaped contrails alone [*Burkhardt and Kärcher*, 2011]. During the entire lifecycle of contrails and contrail cirrus, aviation-related particles can influence the hydrological process of natural cirrus clouds by competing for water vapor and by providing additional ice nuclei. In the shortwave region, the radiative forcing of contrails and

[1]Department of Atmospheric Sciences, Texas A&M University, College Station, Texas, USA.
[2]Joint Institute for Regional Earth System Science and Engineering and Department of Atmospheric and Oceanic Sciences, University of California, Los Angeles, California, USA.
[3]Science Directorate, NASA Langley Research Center, Hampton, Virginia, USA.

0148-0227/12/2011JD017020

contrail cirrus is significantly affected by ice crystal size and shape [*Meerkötter et al.*, 1999]. For this reason, our limited knowledge of ice crystal characteristics in these clouds must be improved in order to more reliably quantify the radiative impact of aviation-induced cloudiness, which is one of the objectives of the Aviation Climate Change Research Initiative (ACCRI) program [*Brasseur and Gupta*, 2010; *Yang et al.*, 2010]. As *Burkhardt and Kärcher* [2011] pointed out, consistent data sets of the optical properties of line-shaped contrails are crucial for further improvement of representations of contrail cirrus processes in models. To help better understand the transition of contrails to contrail cirrus, this study is aimed at obtaining and interpreting climatological statistics of contrail optical and physical properties over a wide geographical area. To obtain statistically significant results, we used collocated data from the Moderate Resolution Imaging Spectroradiometer (MODIS) and the Cloud-Aerosol Lidar with Orthogonal Polarization (CALIOP) on board the Cloud-Aerosol Lidar and Infrared Pathfinder Satellite Observations (CALIPSO) satellite. The lidar adds unique information (e.g., ice crystal habit, accurate height, and physical width and thickness) about contrails that cannot be obtained using imager data alone. Theoretical scattering calculations for several microphysical models were used to further analyze backscattering properties, which are discussed and compared with observational results.

[4] This paper is organized into six sections. After briefly reviewing contrail microphysics in section 2, the methodology of collocated MODIS-CALIOP data analysis is presented in section 3. The analysis results from 2 years of data are presented in section 4. Observational results of the backscattering properties are compared with theoretical predictions and the microphysical properties of contrail ice crystals are discussed in section 5. Section 6 presents the conclusions of the present study.

2. A Brief Review of Contrail Microphysics

[5] *Schumann* [2002] and *Heymsfield et al.* [2010] have reviewed contrail microphysics in some detail. Contrail evolution can be divided into three time phases; the jet (about 20 s), the vortex (about 2 min), and the dispersion (up to hours). Contrails are generated when warm exhaust gases mix with cold ambient air resulting in a liquid saturation process during which the droplets freeze instantly (within 0.1 s). During the vortex phase, contrail ice crystals are trapped in aircraft wing edge generated vortexes and a significant fraction of them may sublimate from adiabatic heating caused by the descending motion of the vortex system. The fraction of crystals surviving the vortex phase depends primarily on the relative humidity, temperature, and aircraft type [*Sussmann and Gierens*, 1999, 2001]. On the basis of in situ sampling of ice particles in fresh contrails (age < 2 min), these particles are usually small with a high number concentration [*Petzold et al.*, 1997; *Baumgardner and Gandrud*, 1998; *Gayet et al.*, 1998; *Goodman et al.*, 1998; *Schröder et al.*, 2000; *Febvre et al.*, 2009]. In many cases, the shapes of these particles have been reported as quasi-spherical [*Gayet et al.*, 1998; *Febvre et al.*, 2009; *Schröder et al.*, 2000], although the limited resolution of particle imagers and optical arrays made it difficult to identify definitive shapes of small particles.

[6] A contrail can persist beyond the vortex phase if the ambient relative humidity with respect to ice exceeds 100%. During the aging phase, ice crystals generally grow in size and the number concentration decreases owing to dispersion [*Poellot et al.*, 1999; *Schröder et al.*, 2000]. A high ice crystal number concentration was found to reside at the contrail core. Larger ice crystals form at the contrail edges from water vapor supplied by humid ambient air, which is consistently confirmed by in situ and remote sensing measurements [*Petzold et al.*, 1997; *Duda et al.*, 1998; *Heymsfield et al.*, 1998; *Knollenberg*, 1972; *Lawson et al.*, 1998]. As large particles fall more quickly than small ones, large ice crystal fall streaks observed as virga (diffuse structures) may occur in aged contrails. The in situ and remote sensing measurements are consistent with the results obtained from large eddy model simulations [*Heymsfield et al.*, 1998; *Jensen et al.*, 1998; *Atlas et al.*, 2006]. Old contrails are similar to surrounding cirrus clouds in terms of mean particle size [*Gayet et al.*, 1996; *Duda et al.*, 1998; *Minnis et al.*, 1998; *Schröder et al.*, 2000]. As aging of contrails and the corresponding increase in particle size take place, ice crystals with complicated shapes become dominant and are consistent with the measured phase functions, which deviate from the spherical particle model [*Gayet et al.*, 1998; *Lawson et al.*, 1998; *Febvre et al.*, 2009]. In situ measurements by particle imaging probes found the shapes of large ice crystals to be either regular, such as bullet rosettes and columns, or irregular [*Gayet et al.*, 1996, 1998; *Heymsfield et al.*, 1998; *Lawson et al.*, 1998; *Febvre et al.*, 2009]. The spatial variations of the microphysical properties within a contrail often make it difficult to derive robust data from in situ measurements.

[7] Lidar is a powerful tool for the detection and characterization of the spatial structure and microphysical properties of cirrus clouds. Particularly, depolarization observations have provided useful information on ice crystal size, shape, and orientation [*Sassen*, 1991]. *Freudenthaler et al.* [1996] used a scanning polarization lidar and found the linear depolarization ratio (LDR, δ), defined as the ratio of the perpendicular to parallel component of lidar backscatter, increases from 0.1 to 0.5 in conjunction with an increase in temperature from −60 to −50°C in the contrail vortex phase (age < 1.6 min). Contrails in the dispersion phase had a LDR of approximately 0.5. *Sassen and Hsueh* [1998] reported that the LDR in contrails ranged from 0.3 to 0.7. Compared to natural cirrus clouds, which normally have δ values in the 0.3–0.5 range, some contrails had unusually large LDRs ($\delta > 0.5$). *Del Guasta and Niranjan* [2001] analyzed 61 contrails and obtained a wider range of δ from 0.33 to 0.82. *Langford et al.* [2005] found that δ tended to be large at the top of contrails, whereas the profile-mean δ was quite small with values of 0.15–0.25. These measurements were limited to either field campaigns or specific areas and temporal periods. The complete statistics of the contrail depolarization properties are yet to be developed.

3. Methodology

3.1. Data

[8] The Aqua and CALIPSO satellites provide collocated observations with a small temporal difference (~75 s). Since contrails are usually thin and narrow, level 1B data with full

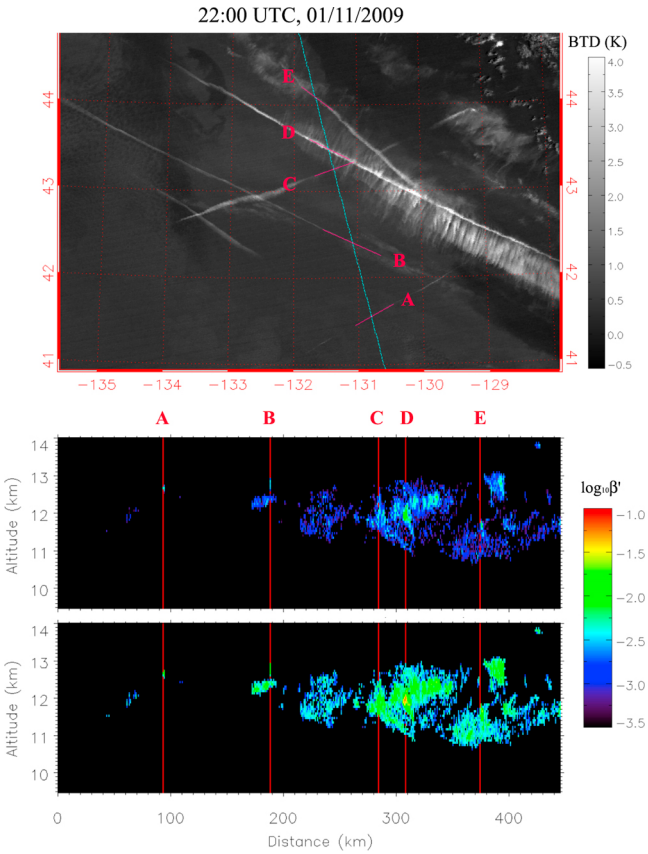

Figure 1. (top) An image of MODIS brightness temperature difference (BTD) between 11 and 12 μm channels over the northeast Pacific on 11 January 2009. Cyan line denotes the locations of MODIS-CALIOP collocated pixels. Magenta line segments denote contrails detected by manual inspection. (middle and bottom) CALIOP profiles of attenuated total and perpendicular backscattering coefficients (km^{-1} sr^{-1}), respectively, at 532 nm wavelength corresponding to the scene in the MODIS image. Red vertical lines denote contrail locations detected by MODIS image analysis. Only cloudy cross-sectional elements are plotted.

spatial resolution (1 km horizontal resolution for MODIS infrared channels) are necessary for this study. For CALIOP, we used data degraded by averaging the original level 1B data to obtain uniform horizontal and vertical resolutions of 1 km and 60 m. Contrail locations were determined from the analysis of an Aqua-MODIS image, while the collocated CALIOP data were employed to identify the contrails. We used CALIOP data obtained from quasi-nadir (0.3° off) lidar pointing for the year 2007 and off-nadir (3° off) pointing for 2009. A comparison study based on the 2 year data sets is conducted here to determine the potential effects of particle orientation on lidar-derived properties.

[9] The selected target region for this study is between latitudes from 20°N to 80°N and longitudes from 180°W to 60°E, and includes the areas where contrails most frequently occur [e.g., *Burkhardt and Kärcher*, 2011]. To reduce the demand on computational resources and the data analysis workload, we acquired MODIS and CALIOP level 1B data only for cases with a high possibility of contrails appearing over the MODIS-CALIOP collocated pixels. Daytime (afternoon) orbits were chosen for the case selection, because we used MODIS true color images, composed of three visible wavelength channels with a 500 m spatial resolution, available from the MODIS Rapid Response System (http://rapidfire.sci.gsfc.nasa.gov/). Over the oceans, isolated contrails can be easily identified. Also, the observing contrail shadows made it possible to find contrails over bright polar region ice sheets or homogeneous low-cloud decks. Contrails occur frequently in or near high-level cloud systems [*Sassen*, 1997], because the occurrence of contrails is prevalent when the relative humidity is high. Therefore, we also acquired data for cases in which cirrus clouds appeared around the centerline of MODIS images.

3.2. Detection of Contrails in MODIS Images

[10] To detect contrails we used the brightness temperature difference (BTD) between the MODIS 11 μm and 12 μm channels, because this method increases contrail visibility [e.g., *Minnis et al.*, 2005] owing to the typically small particles within contrails and the corresponding low optical depths. The locations, azimuth directions, lengths, and rough estimates of age were manually determined for individual contrails. An automated contrail detection algorithm works well for isolated linear features, but the efficient detection of old-aged, irregular-shaped contrails is rather involved [*Minnis et al.*, 2005]. For our purpose, manual detection was used to recognize particular patterns; to interpolate disconnected, intermittent contrail segments; and to identify contrails with transformed shapes. As noted by *Kärcher et al.* [2009], the BTD approach will miss many of the thinnest (optical depths less than 0.1 or so), thus, such contrails are not completely represented in this study.

[11] Figure 1 (top) shows an example of a BTD image, with five hand-drawn lines (denoted by A, B, C, D, and E) superimposed on possible contrails that cross a CALIPSO track. Collocated MODIS-CALIOP pixels (denoted by cyan lines) were determined by using the geolocation information recorded in MODIS and CALIOP data sets. Contrails A and B can be regarded as young because of linear shapes with sharp edges, but contrails C, D, and E are more likely to be mature. Contrail C is dim near the MODIS-CALIOP collocated pixel but its eastward and westward extensions suggests the possibility that it could be detectable in a CALIOP profile. Contrail D has a distinct artificial cloud appearance and a width of about 5 km near the MODIS-CALIOP collocated pixel where the large BTD indicates a moderate optical thickness (roughly 1) and/or small particle sizes [e.g., *Betancor-Gothe and Grassl*, 1993]. Other cloud features could be natural cirrus clouds or significantly aged contrails (contrail cirrus) that no longer have a distinct contrail appearance. In practical data processing, we found many dim features that might be contrails, such as indistinct lines embedded in extended cirrus clouds, extrapolated parts from distinct linear contrails, and faintly thin features between two distinct contrail segments, both of which could be associated with the same aircraft. We considered these features as contrails at this stage of analysis, because the subsequent lidar data analysis can better identify a multi-layered cirrus cloud system as well as optically thin cirrus. Around contrail B, we see a dim, linear-shaped feature, spread to a width of more than 10 km and located in the same direction as contrail B, which appears to be an aged

contrail. However, we discarded this type of feature because of low confidence. For each contrail, we estimated a length from the beginning to the end points of a contrail feature that appeared continuous in the MODIS image. The computed length can be considered as a minimum estimate, because in addition to frequent contrail intermittency, the exact beginning and end points might have occurred outside the MODIS image limits.

[12] Despite possible ambiguities, we classified detected contrails into three types; young, mature, and old on the basis of the morphology in terms of contrail width, shape (linear or transformed shape), and edge sharpness. A young contrail was identified by four criteria: a linear shape, sharp edges, a width approximately less than 3 km, and a maximum distance less than 200 km from the head. Assuming a flight speed of 900 km h^{-1} [*Penner et al.*, 1999], the distance from the head corresponds to an approximate age of less than 13 min. The width of this contrail type was frequently smaller than the MODIS pixel size (1 km) such that the contrail appeared as a dotted or dashed line in the BTD image. The type separation of mature and old contrails is more uncertain. A relatively distinct feature with slightly diffusive edges, a linear shape, and an approximate width less than 7 km was classified as a mature contrail. We observed a tendency for mature contrails to have larger BTD values than old contrails. The remaining contrail features were all classified as old contrails, which do not have a distinct line-like shape on a small spatial scale (roughly 50 km); however, on a large scale (>100 km), the linear (or curved) shape was apparent and could be easily distinguished from natural cirrus.

[13] Age estimation of mature and old contrail types has been difficult, partly because the width depends not only on age, but also on ice-supersaturated layer thickness and wind shear perpendicular to the contrail direction [*Jensen et al.*, 1998]. If a thick contrail has evolved in a deep ice-supersaturated layer, it can spread horizontally by both wind shear and aging. Using scanning lidar measurements, *Freudenthaler et al.* [1995] derived a horizontal spreading rate ranging from 18 to 140 m min^{-1} in the initial 1 h of the contrail life cycle. Observational results with support by model simulations suggest that the contrail width at 1 h of age may vary from 1 to 10 km [*Jensen et al.*, 1998; *Unterstrasser and Gierens*, 2010]. Taking these factors into consideration, the ages of our manually classified mature contrails are likely to be between 13 min and 1–2 h.

[14] Excluding the very new (age < 2 min) and short-lived contrails that disappear in dry air, essentially all of the contrails we analyzed could be considered persistent contrails. From the perspective of climatic effects, persistent contrails are more important than short-lived contrails, because the global coverage of short-lived contrails has been estimated to be extremely small [*Ponater et al.*, 1996].

3.3. CALIOP Data Processing and Identification of Contrails

[15] The CALIOP data include the total and perpendicular attenuated backscattering coefficients at a wavelength of 532 nm denoted by β'_{532} and β'_{532s}, respectively, and the total attenuated backscattering coefficient at 1064 nm (β'_{1064}). In preprocessing, we identified clouds as cross-sectional segments where $\beta'_{532} + \beta'_{1064} > 0.003$ $km^{-1}sr^{-1}$. Any isolated feature with a width less than 1 km and a thickness less than 60 m was regarded as noise. To obtain signals with regards to particulates (e.g., ice crystals), the scattering contribution by air molecules and attenuation by air molecules, ozone, and particulates were corrected by using the methods developed in previous studies (C. A. Hostetler et al., CALIPSO algorithm theoretical basis document: PC-SCI-201, 2006, http://www-calipso.larc.nasa.gov/resources/project_documentation.php, hereinafter referred to as Hostetler et al., online document, 2006). When solving the lidar equation, we initially assumed an extinction-to-backscattering (lidar) ratio (S) of 25 sr, which was a reasonable average value for contrails and optically thin natural cirrus [*Sassen and Comstock*, 2001; *Langford et al.*, 2005]. According to previous studies, the lidar ratio depends on both cloud type and temperature. We will revisit this issue in section 5. Referring to several studies [e.g., *You et al.*, 2006; Hostetler et al., online document, 2006], we assumed the multiple scattering parameter to be $\eta = 0.7$, which was included in an effective lidar ratio $S' = \eta S$. With the initial assumption of $S = 25$ sr, the lidar equation is solved by a simple iterative algorithm from the top to the bottom of a cloudy layer. If either of the following occurs, a solution diverges or a negative value of the backscattering coefficient is obtained, the lidar ratio is adjusted slightly and the entire cloud layer is recalculated. Total, parallel, and perpendicular backscattering coefficients (β_{532}, β_{532p}, β_{532s}) and extinction coefficients (κ_{532}) at a wavelength of 532 nm were calculated for each cross-sectional element. Optically thin elements with $\kappa_{532} < 0.04$ km^{-1} were regarded as noncloudy and removed from subsequent analysis. Thus, the minimum optical thickness of a cloud layer is 0.0024.

[16] Uncertainties in the backscattering, extinction coefficients, and optical thickness (τ) are primarily from noise in the CALIOP data and possible variations of the effective lidar ratio. Although the latter may arise as a result of variations in the lidar ratio and the effects of multiple scattering, we assumed a constant effective lidar ratio for each cloud column. The solution algorithm tends to be unstable at the lower part of thick cloud layers. Thus, we confined our analysis to the upper part with $\tau < 1.25$ from the top of the uppermost cloud layer. Although quantitative estimation of the uncertainty in τ is complicated and needs further careful investigation, an improvement of the retrieval algorithm or ultimately a better lidar technique (e.g., high spectral resolution lidar) will be needed to reduce the uncertainty in τ. In this study, our major concerns are statistical properties and a possible dependence on ambient conditions. For the CALIOP configuration, the influence of multiple scattering on cirrus LDR is less than 0.006 when $\tau < 1.2$ [*Reichardt and Reichardt*, 2003]. Previous passive remote sensing studies [e.g., *Meyer et al.*, 2002; *Palikonda et al.*, 2005] indicate that 80% or more line-shaped contrails have $\tau < 0.5$, thus, the multiple scattering effect is expected to be very small.

[17] With the help of the location information determined from the MODIS data analysis, contrails were searched in the CALIOP profile. Figure 1 (middle and bottom) shows CALIOP profiles in a sample case corresponding to the MODIS image shown in Figure 1 (top). Noncloudy elements with weak backscattering signals are masked in the plots.

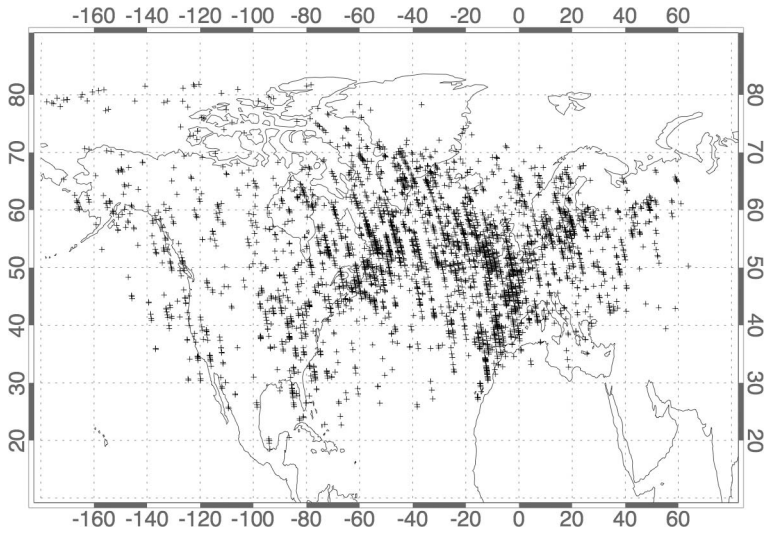

Figure 2. Geographical locations of contrails analyzed in this study. Each single cross denotes a contrail location identified by MODIS and CALIOP data analysis.

Contrails were identified on the basis of the limited vertical extent with substantial backscattering, as compared to surrounding cirrus. Red vertical lines in the plots denote contrail locations detected by the MODIS image analysis. Young contrails A and B were isolated from cirrus clouds having confined widths within 1–2 km. The vertical extent is approximately 250 m for A and 450 m for B. A cirrus cloud with a width of about 30 km was present just beneath contrail B and a dim feature in the MODIS image was found. Contrail C is not clearly exhibited in this profile so that we rejected the sample. Contrail D is embedded in cirrus, while contrail E extends from cirrus. Both are mature with moderate vertical and horizontal extents.

[18] Since contrails are not always oriented perpendicular to the CALIOP track, the apparent contrail width (W') shown in lidar profiles is corrected by considering an angle (ϕ) between the contrail and CALIPSO track directions. A corrected width is given by

$$W = W' \sin \phi. \tag{1}$$

Contrail identification was done semiautomatically with contrail core centers nominally identified by maxima in β_{532} within 7 km from the location diagnosed in the MODIS analysis. The 7 km tolerance is from errors due to the hand drawing of lines over MODIS images, uncertainties of the geolocation values provided in the MODIS and CALIOP data, and location differences between peaks of the BTD and the β_{532}. Subsequently, a cluster of cloudy elements surrounding the core center was identified. Determining contrail boundaries embedded in or extending from cirrus could produce errors. The contrail width was restricted not to exceed 3, 7, and 21 km for young, mature, and old contrails, respectively. We assumed that β_{532} within a contrail should decrease with increasing distance from core center. The surrounding cirrus volumes are discriminated as cross-sectional elements with $\beta_{532}(\Delta x, \Delta z)$ larger than a threshold $\beta_{\min}$, where Δx and Δz are horizontal and vertical distances from the core center. The threshold is given by the two-dimensional Gaussian distribution as follows:

$$\beta_{\min} = \frac{\beta_{peak}}{\pi \sigma_x \sigma_z} \exp\left\{ -\frac{1}{2} \left[\left(\frac{\Delta x}{\sigma_x} \right)^2 + \left(\frac{\Delta z}{\sigma_z} \right)^2 \right] \right\}, \tag{2}$$

where β_{peak} is the β_{532} value at core center. The standard deviations σ_x and σ_z are estimated from horizontal and vertical profiles of β_{532} and the contrail age and are adjusted after manual inspection for each contrail. In practice, the determination of contrail boundaries was difficult when a contrail with no distinct clustering of large β_{532} was embedded in an optically thick cirrus layer. Such cases were excluded from subsequent analysis resulting in rejection of about 21% of the contrails detected in the MODIS data analysis.

[19] The properties of cirrus clouds adjacent to contrails are of particular interest because they appear under similar meteorological conditions. We defined neighboring cirrus as those present within a horizontal distance of 150 km and a vertical distance of 1.5 km from the contrail core center. The neighboring cirrus clouds in our analysis were not necessarily natural. Some could be old-aged contrails that no longer had a contrail-like shape, while others could be cirrus indirectly influenced by either contrail particles or gases and aerosol particles from aircraft exhausts.

[20] The backscattering coefficients were separately averaged over cross-sectional elements of each contrail and the neighboring cirrus clouds. The contrail/cirrus-integrated LDR (δ) was computed by

$$\delta = \langle \beta_{532s} \rangle / \langle \beta_{532p} \rangle, \tag{3}$$

where an angle bracket denotes integration over cross-sectional elements. Other analyzed quantities include τ, latitude, altitude, width, height, temperature, and relative humidity with respect to ice (RH_{ice}). When computing τ statistics, each contrail sample was weighted by the width W. We used meteorological data (pressure, temperature, relative

Table 1. Summary Statistics of Geographical, Geometrical, and Meteorological Properties of All Detected Contrails Analyzed in This Study[a]

Property	Value
Latitude (°N)	51.9 (10.3)
Contrail-top altitude (km)	10.9 (1.0)
Width (km)	6.5 (4.8)
Thickness (km)	0.67 (0.32)
Length (km)	264 (294)
Contrail-top temperature (°C)	−54.6 (5.3)
RH_{ice} (%)	126 (26)

[a]Averages are shown with standard deviations in parentheses. RH_{ice} denotes relative humidity with respect to ice.

humidity, and molecular and ozone number densities) included in the CALIPSO data set, which was originally obtained from the NASA Global Modeling and Assimilation Office (GMAO) meteorological analysis (Hostetler et al., online document, 2006).

4. Observational Results

4.1. Geography, Geometry, and Meteorology

[21] Figure 2 shows geographical locations of a number of detected contrails. Many of them are located over the North Atlantic region, especially over the major flight corridors between the United States and Europe. High concentrations are noted in Western Europe, the southern part of Greenland, and the eastern part of North America. It should be noted that our data sampling is neither seasonally nor spatially homogeneous. Aqua and CALIPSO satellites cover high-latitude regions, but winter data were not available over polar regions on the MODIS Rapid Response System website. The contrails in our analysis are concentrated over the oceans; however, coverage of the line-shaped contrails estimated from climate model simulations is higher over land in the United States and Europe than those over oceanic regions [*Burkhardt and Kärcher*, 2011].

[22] Table 1 and Figures 3 and 4 summarize the statistics obtained with regards to geometry and meteorological conditions. Detected contrails mostly appear in the uppermost part of the troposphere with their tops below the tropopause by 0–2 km with an average top altitude of about 10.9 km. Figure 3a shows that the average contrail-top altitude decreases with increasing latitude. The top altitude z (km) and latitude θ (°) can be represented by a least squares fit as follows:

$$z \approx 12.5 - 0.035\theta, \tag{4}$$

with a root-mean-square error of 0.96 km and a correlation coefficient of −0.37 between z and θ. We found that in many cases, contrail tops were higher than nearby cirrus (Figure 4a). Although the standard deviation is as large as 0.5 km, the average difference is about 0.2 km. Higher contrail tops suggest a possibility that aircraft generate contrails at altitudes greater than the cirrus tops, while our inability to detect a thin contrail embedded within a thick cirrus may influence the overall results for contrail-top altitude. Figure 4b shows areal fractional cover of cirrus in the near field, that is, how much of the atmospheric column near a contrail is covered by cirrus. In 23% of all cases, cirrus covered over 95% of the area near a contrail. In 80% of cases, cirrus covered over 50% of the surrounding area. These results, similar to those from land surface observations [*Minnis et al.*, 2003], suggest that when a contrail appears, cirrus clouds are likely to appear near the contrail in view of the fact that sufficient humidity is present to control the occurrence of both contrail and cirrus. Although the surrounding cirrus clouds could be contrail cirrus from older contrails in some cases, the available information was insufficient to determine whether the surrounding cirrus clouds were anthropogenic or natural.

[23] In general, detected contrails appear in cold and supersaturated environments. The average contrail-top temperature was −54.6°C, almost identical to the temperature (−55°C) at extratropical cruising altitudes near 200 hPa [*Kärcher et al.*, 2009]. The majority of contrails were found in a temperature range between −42 and −63°C, which indicates that the contrail formation is primarily related to ice crystal nucleation by homogeneous freezing of liquid droplets. Although the relative humidity from model analysis involves uncertainty, the midlevel RH_{ice} values yield an average of 126% and are distributed as shown in the histogram of Figure 4c. Of all detected contrails, 13% occurred in subsaturated conditions (RH_{ice} < 100%) according to the GMAO analyses and are believed to have been dissipating by evaporating ice particles. However, the majority of detected contrails are considered persistent with an ambient RH_{ice} higher than 100%. Although the upper tropospheric humidity from GMAO model analysis involves uncertainty and is debatable, highly supersaturated air (RH_{ice} > 150%), a

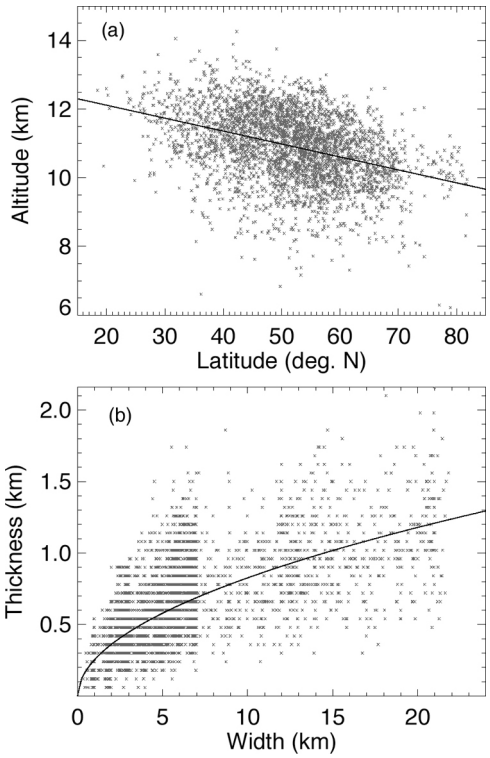

Figure 3. Scatterplots of (a) top altitude of all detected contrail and latitude and (b) geometrical thickness and width. Least squares fits of a line and a power law curve are superimposed in Figures 3a and 3b, respectively.

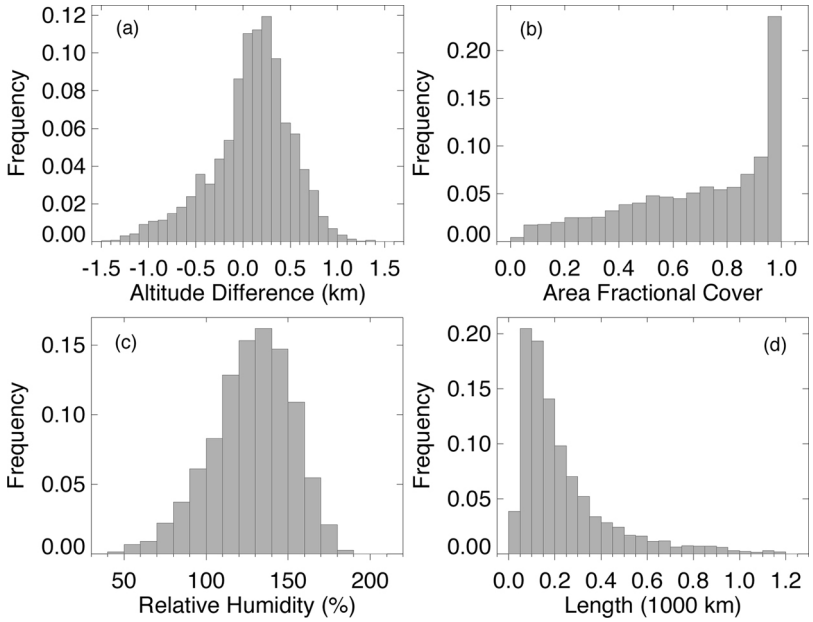

Figure 4. Histograms of (a) cloud top altitude difference between detected contrail and neighboring cirrus, (b) area fractional cover of cirrus in the near field of contrail, (c) relative humidity with respect to ice at midlevel within contrail, and (d) contrail length.

favorable condition for the formation of natural cirrus, accounted for about 22% of the cases analyzed. The largest contrail population (65%) was found in moderately supersaturated air (100% < RH_{ice} < 150%).

[24] The contrail average horizontal width obtained from this analysis is 6.5 km with an average thickness of 0.67 km. Figure 3b shows a scatterplot of thickness and width. Frequency discontinuities around the 3 and 7 km widths occur because we have limited contrail widths by using different maximum values for young and mature contrails, and the discrepancies suggest a need for improvement in contrail boundary identification. Nevertheless, there is a clear positive correlation between thickness (H in km) and width (W in km). The superimposed curve in Figure 3c is a least squares fit given by

$$H \approx 1.29W^{0.513}, \tag{5}$$

with a root-mean-square error of 0.26 km. Both thickness and width may increase with aging. At the end of the vortex phase (about 2 min), contrails can grow vertically to 100–300 m in depth with little horizontal spreading [*Schumann*, 2002]. In addition, ice crystals falling below the bottom of a supersaturated layer would evaporate so that the depth of the ice-supersaturated layer would limit the vertical development [*Freudenthaler et al.*, 1995]. However, the horizontal spreading is not subject to this limitation in view of the fact that the width is approximately proportional to the square of the thickness.

[25] Figure 5 shows the average thickness of detected contrails as a function of midlevel RH_{ice} and width. There is a tendency for the thickness to increase with increasing midlevel RH_{ice}, because thick contrails evolve in highly supersaturated air owing to the faster growth and sedimentation of large ice particles. The horizontal spreading of persistent contrails is typically determined by wind shear [*Jensen et al.*, 1998; *Kärcher et al.*, 2009; *Unterstrasser and Gierens*, 2010]. If supersaturation is present in a thick layer, wind shear can effectively spread the contrail in the horizontal direction, and at the same time contrail vertical cross sections may be inclined, a feature we often observed in the CALIOP profile particularly for old contrails. Thus, the contrail width depends on the ice-supersaturated layer depth, wind shear, as well as age. Table 3 presents the geometrical size statistics for the three contrail types: young, mature, and old.

[26] Estimates of width and thickness depend on the threshold for contrail boundary determination. The *Kärcher et al.* [2009] model simulation results indicate that the average width of a contrail between 2 min and 4 h old can be as large as 18–19 km, if the optically thin parts of contrails are included. The average width (6.5 km) in our results is only one third of the value presented by *Kärcher et al.* [2010], which attests to the inherent difficulty in defining

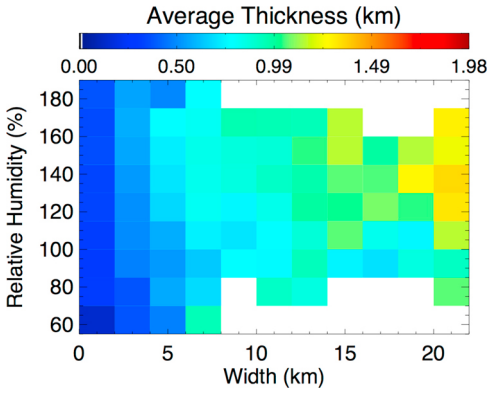

Figure 5. Average geometrical thickness as a function of width and relative humidity with respect to ice.

Table 2. Summary Statistics of Lidar-Derived Optical Properties for All Detected Contrails and the Neighboring Cirrus Clouds at a Wavelength of 532 nm[a]

	Contrails	Neighboring Cirrus Clouds
Quasi-Nadir Observations: 2007		
β_{532} (km^{-1} sr^{-1})	0.0232 (0.0170)	0.0138 (0.0076)
δ	0.393 (0.127)	0.319 (0.085)
τ	0.256 (0.189)	-
Number of cases	1484	1425
Off-Nadir Observations: 2009		
β_{532} (km^{-1} sr^{-1})	0.0191 (0.0145)	0.0102 (0.0053)
δ	0.439 (0.092)	0.409 (0.052)
τ	0.190 (0.153)	-
Number of cases	1904	1738

[a]Optical properties listed are total backscattering coefficient (β_{532}), LDR (δ), and optical thickness (τ). Averages are shown with standard deviations in parentheses.

Table 3. Summary Statistics of Lidar-Derived Optical Properties for Three Contrail Types

	Young Contrails	Mature Contrails	Old Contrails
Quasi-Nadir Observations: 2007			
β_{532} (km^{-1} sr^{-1})	0.0270 (0.0203)	0.0242 (0.0167)	0.0174 (0.0112)
δ	0.410 (0.128)	0.392 (0.130)	0.377 (0.120)
τ	0.274 (0.228)	0.275 (0.209)	0.240 (0.163)
Number of cases	422	664	398
Off-Nadir Observations: 2009			
β_{532} (km^{-1} sr^{-1})	0.0258 (0.0169)	0.0196 (0.0137)	0.0142 (0.0125)
δ	0.446 (0.105)	0.439 (0.092)	0.435 (0.084)
τ	0.240 (0.180)	0.205 (0.181)	0.162 (0.114)
Number of cases	333	1026	545
Geometrical Properties: 2007 and 2009			
Width (km)	2.5 (0.6)	5.1 (1.6)	12.3 (5.2)
Thickness (km)	0.48 (0.19)	0.64 (0.27)	0.87 (0.38)
Length (km)	205 (240)	260 (299)	321 (312)

contrail boundaries. On the other hand, the limited horizontal resolution of CALIOP can produce positive bias in the width, because the contrail volume may only partly cover a cross-sectional element for a CALIOP observation. The partial coverage may introduce a positive bias of 0–2 km in the width estimate. If we assume an average bias of about 1 km, the corrected average widths of young, mature, and old contrails should have been 1.5, 4.1, and 11.3 km, respectively. Lidar measurements in southern Germany [*Freudenthaler et al.*, 1995] revealed widths of persistent contrails (age < 60 min) to be 1.5–3 km, a range consistent with our results.

[27] The mean length of detected contrail is 264 km with a large standard deviation. A length histogram in Figure 4d shows a strongly skewed distribution having a mode at 50–100 km. Contrail length statistics are considered to represent the horizontal extent of a continuously ice-supersaturated region at cruise altitude. Approximately 11% of our samples were longer than 500 km. Note that contrails longer than about 500 km could be underestimated in our analysis.

4.2. General Statistics of Lidar-Derived Optical Properties

[28] Table 2 summarizes the statistics of lidar-derived optical properties for all detected contrails and the neighboring cirrus clouds. Table 3 lists type-specific contrail properties, while Figure 6 visually displays average and standard deviation values. As shown, contrails exhibit much larger backscattering coefficients by about twofold and slightly higher LDRs than neighboring cirrus clouds. The average LDRs are 0.39 and 0.44 in quasi-nadir and off-nadir observations, respectively. The typical values of contrail LDRs lie in the range of 0.3–0.55, which is consistent with previous ground-based lidar measurements for dispersion phase contrails [*Freudenthaler et al.*, 1996; *Sassen and Hsueh*, 1998; *Del Guasta and Niranjan*, 2001; *Sussmann and Gierens*, 2001]. The same LDR range is also typical for natural cirrus ice crystals [*Sassen and Benson*, 2001; *Sassen and Zhu*, 2009]; however, the nonnegligible differences in depolarization between contrails and neighboring cirrus clouds indicate variations in the microphysical properties. Young contrails were found to have large backscattering coefficients and high LDRs implying high ice crystal number concentrations. Assuming the backscattering phase function value to be about the same, a significantly high number concentration should make up for the large backscattering coefficients and compensate for the cross section of small ice particles dominant in young contrails in terms of backscattering efficiency. Old contrails had smaller

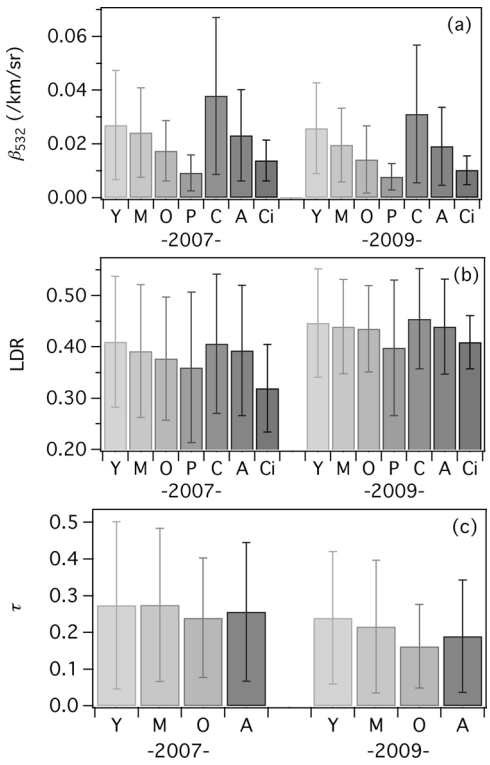

Figure 6. Averages of (a) backscattering coefficients, (b) linear depolarization ratios (LDRs), and (c) optical thicknesses at 532 nm. Error bars denote standard deviations. Y, M, and O denote young, mature, and old contrails. P and C denote contrail peripheries and cores. Statistics for all detected contrails and neighboring cirrus clouds are denoted by A and Ci, respectively. Statistics were computed for the years 2007 and 2009 for which CALIOP had different off-nadir angles of 0.3° and 3°, respectively.

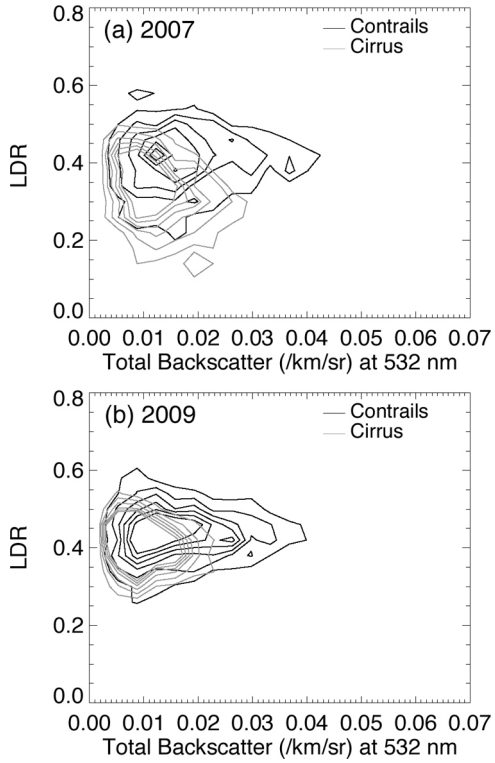

Figure 7. Two-dimensional frequency distributions of LDR and total backscattering coefficient at 532 nm of detected contrails and neighboring cirrus clouds for (a) off-nadir measurements in 2007 and (b) quasi-nadir measurements in 2009. Contour lines are drawn for equally spaced frequency values.

backscattering coefficients and lower LDRs with values close to those of the neighboring cirrus clouds. Thus, aged contrails and neighboring cirrus clouds could have similar microphysical properties.

[29] Contrail cores are known to contain a high number concentration of small particles, while fall streaks contain large particles with small number concentration [*Heymsfield et al.*, 1998; *Lawson et al.*, 1998; *Atlas et al.*, 2006; *Unterstrasser and Gierens*, 2010]. For each contrail, we classified the cross-sectional elements into core or periphery areas. A core was defined as having a larger β_{532} than the median value, and the remaining elements were identified as peripheries. As shown in Figure 6, contrail cores have higher average LDRs than peripheries. Thus, it appears that backscattering by small particles in the cores is strongly depolarized.

[30] Specular reflections from the smooth faces of ice particles can produce strong backscattering with little depolarization. Large plates (diameter > 100 μm) tend to fall and flutter with their major axes oriented horizontally. Thus, it is generally accepted that the strong backscattering with weak depolarization observed by vertically pointing lidar is generated by horizontally oriented plates [*Sassen and Benson*, 2001]. If the lidar is pointing a few degrees off nadir, the effects of specular reflection would be significantly reduced. As shown in Figure 6, quasi-nadir observations yield a larger average β_{532} and a lower average δ than off-nadir observations and these properties are particularly noticeable in cirrus clouds. Differences in the average δ by the pointing angle are about 11% for contrails and as large as 25% for neighboring cirrus clouds. For young, mature, and old contrails, the corresponding differences are 8%, 11%, and 15%, respectively. The influence of horizontally oriented plates is evidently stronger in old contrails and cirrus clouds than in young contrails, which can be attributed to particle size differences by age and between contrails and neighboring cirrus.

[31] The average optical thicknesses (τ) are 0.24 in quasi-nadir and 0.19 in off-nadir observations. The difference of approximately 30% measured by the pointing angle reveals the average backscattering coefficient variation from assuming a constant lidar ratio independent of the pointing angle. The optical thickness standard deviation was almost the same as the average, indicating a large diversity in this parameter. The partial coverage by a contrail over cross-sectional elements in a lidar profile can introduce a positive bias in the width and a negative bias in the optical thickness. For instance, a contrail width of 1.5 km can be identified as 2 or 3 km in the CALIOP data analysis and the corresponding mean optical thickness can be underestimated by 33–100%. The relative impact of partial coverage should be larger for narrower contrails. Considering this effect, young contrails should have larger optical thicknesses than old contrails, as demonstrated by the large eddy model simulations [*Unterstrasser and Gierens*, 2010] mentioned previously.

[32] Figure 7 shows two-dimensional histograms of total backscattering coefficients and LDRs. Detected contrails generally show no significant correlation between the two parameters, but a negative correlation is depicted for cirrus clouds. In quasi-nadir observations (Figure 7a), a significant fraction (38%) of cirrus clouds have $\delta < 0.3$ associated with strong backscattering; however, only 18% of contrails have $\delta < 0.3$. In previous quasi-nadir observations studies [*Hu et al.*, 2007; *Cho et al.*, 2008], the negative correlation was typical for cold ice clouds. Our results suggest the presence of horizontally oriented plates in many cirrus cases. In the off-nadir observations (Figure 7b), the contrail LDR has a narrow distribution between 0.3 and 0.55, but contrails and the neighboring cirrus rarely have $\delta < 0.3$. The LDR of contrails does not strongly depend on the pointing angle; therefore, contrails may have fewer horizontally oriented particles than neighboring cirrus. Further discussion will be given in section 5.4.

[33] The high δ values in the majority of detected contrails are consistent with the results for persistent (age > 2 min) contrails noted by *Freudenthaler et al.* [1996]. Also, *Del Guasta and Niranjan* [2001] have reported rare cases of aged contrails with $\delta < 0.25$, in agreement with our results. Under low ambient relative humidity, *Sassen* [1979] and *Sussmann* [1997] reported halos and perihelions in the aged (>30 min) contrails and predicted horizontally oriented hexagonal plates with diameters of 300–2000 μm. Although our results support the presence of horizontally oriented plates in contrails, the population fraction is expected to be smaller than in neighboring cirrus.

4.3. Dependence of LDR on Altitude, Temperature, and Thickness

[34] Figure 8 shows averages and standard deviations of LDR for each range of altitude, thickness, and temperature. The depolarization is stronger at higher altitudes (Figure 8a).

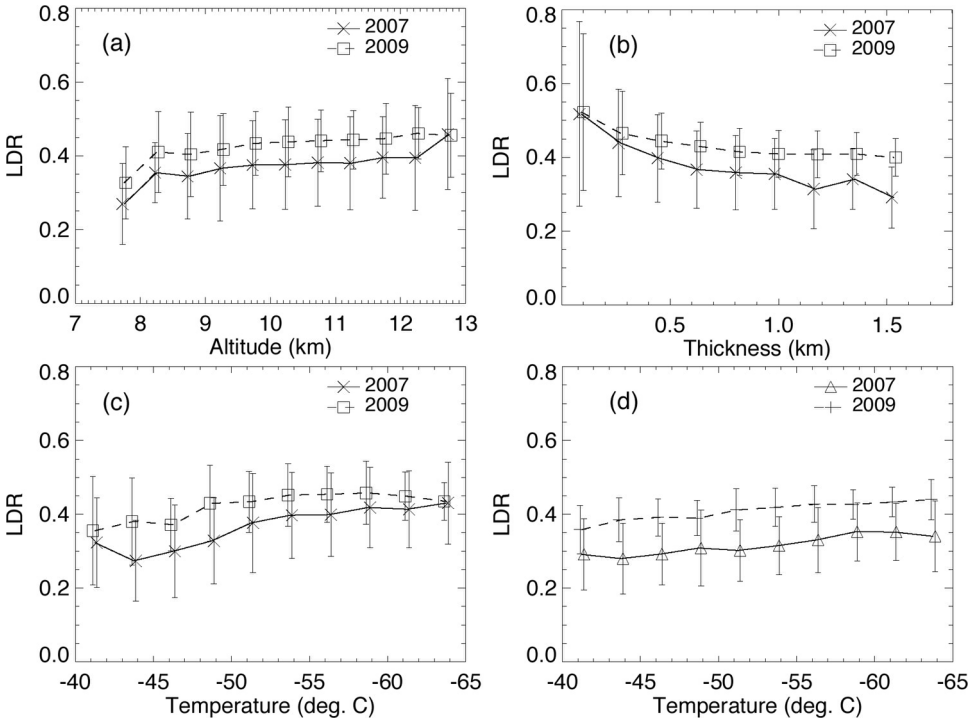

Figure 8. Averages and standard deviations of LDR for each range of (a) altitude, (b) geometrical thickness, and (c) midlevel temperature for detected contrails. (d) Same as Figure 8c but for neighboring cirrus clouds.

LDR is high in geometrically thin contrails (Figure 8b), which can be considered as relatively young contrails, in particular, many contrails that are geometrically thinner than 0.8 km exhibit an LDR larger than 0.6. A steady increase in LDR with decreasing temperature (Figure 8c) is similar to that of neighboring cirrus (Figure 8d). Similar temperature dependencies have been reported in previous observational studies for natural cirrus clouds [*Sassen and Comstock*, 2001; *Reichardt et al.*, 2002; *Sassen and Zhu*, 2009]. According to model predictions, ice crystals have large sizes when the ambient temperature is high [*Unterstrasser and Gierens*, 2010]. Large particles formed at higher temperatures appear to be associated with weaker depolarization.

[35] Our results show that larger LDRs were generally found under the conditions of predominant smaller particles associated with geometrically thin, young contrails, at the contrail core having low temperatures. In section 5, we will present the microphysical interpretation of the results discussed in this section.

4.4. Optical Thickness

[36] Figure 9 shows a histogram of the optical thickness of detected contrails, computed by weighting each sample with the contrail width. Horizontally oriented particles have less influence on off-nadir observations and the results are more likely to be statistically representative. In off-nadir observations, about 34% of the detected contrails have $\tau < 0.1$ with the highest frequency of occurrence shown at $\tau = 0.05$–0.1. The mean optical thickness is 0.19 with a median value of approximately 0.14. A very small fraction (<0.3%) has $\tau > 1$. Thick contrails with $\tau > 0.5$ occupy 5% in off-nadir and 10% in quasi-nadir observations. Fitted curves in

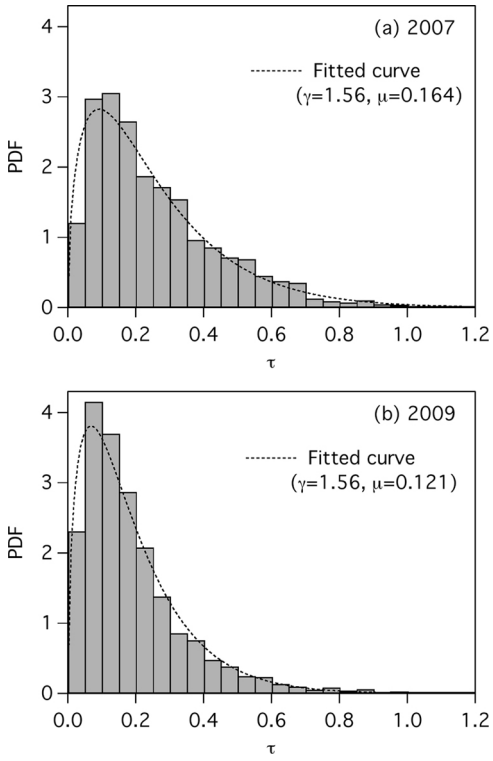

Figure 9. Histograms of optical thickness of detected contrail obtained from measurements in (a) 2007 and (b) 2009. Fitted curves are also shown, where probability density function (PDF) of the Gamma distribution is assumed.

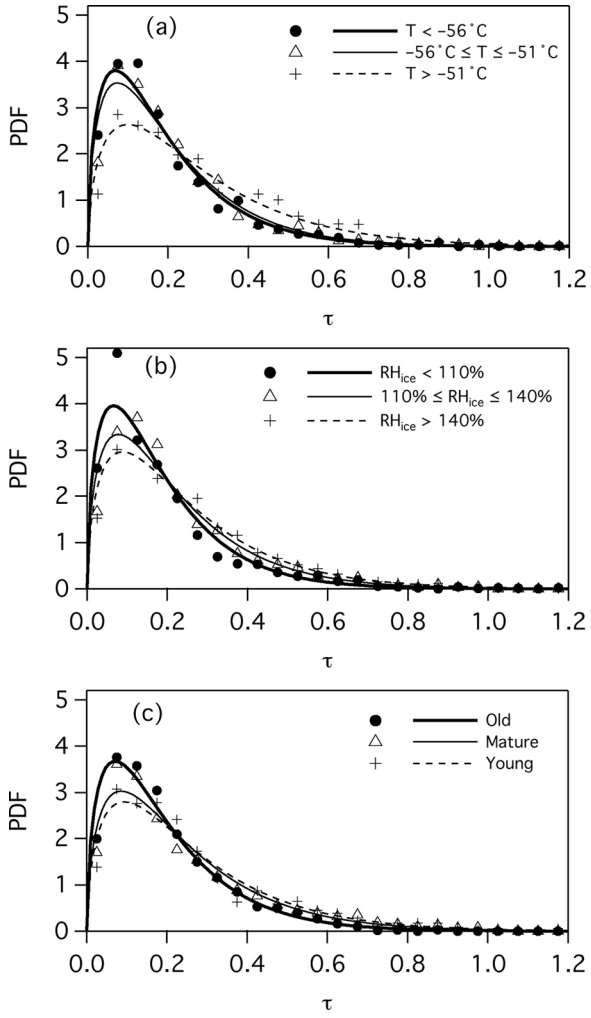

Figure 10. PDFs of optical thickness for (a) different temperature ranges, (b) different ranges of relative humidity with respect to ice, and (c) old, mature, and young contrails. Marks denote directly calculated values from data, and curves denote PDFs modeled by the Gamma distribution.

Figure 9 are the probability density functions (PDFs) represented by the following Gamma distribution:

$$f(\tau) = \frac{(\tau/\mu)^{\gamma-1}\exp(-\tau/\mu)}{\mu\Gamma(\gamma)}, \qquad (6)$$

where Γ is the Gamma function and γ and μ are the shape and scale parameters. For measurements in both 2007 and 2009, the coefficient of variation (standard deviation divided by the mean) g is nearly equal to 0.8, and we define $\gamma = 1/g^2 = 1.56$ for simplicity.

[37] The large τ range is in line with previous observations [e.g., *Minnis et al.*, 2005]. However, the off-nadir averages are shown to be between those determined from passive satellite retrievals: larger values over the United States [*Palikonda et al.*, 2005] while smaller values over Europe [*Meyer et al.*, 2002]. However, comparison with other data sources is not straightforward partly because any inferred τ PDF is instrument specific. *Kärcher et al.* [2009] compiled the optical thickness estimates of persistent contrails obtained from satellite observations using passive sensors, ground/aircraft-based lidar measurements, and model simulations. According to their results, a typical mean of optical thickness is approximately 0.2. Compared with previous studies, the current results seem reasonable considering the geographical and seasonal variations. Model simulations predict a substantial fraction of 20–50% of subvisual contrails ($\tau < 0.02$) [*Kärcher et al.*, 2009, 2010], but our analysis appears to miss a large number of them, which may be caused by inability to detect subvisual contrails in our methodology on the basis of infrared BTD and satellite lidar backscattering analysis. It should be noted that the present results would be useful only when the part of the PDF for subvisual contrails is not concerned. On the other hand, thick contrails with $\tau > 0.5$ are so rare that it is unlikely that the upper limit at $\tau = 1.25$ in the present algorithm would significantly influence overall results.

[38] Figure 10 shows the PDFs of τ for each range of temperature and relative humidity as well as for young, mature, and old contrails. Fitted curves were determined assuming $\gamma = 1.56$, where $g = 0.72$–0.87 (see equation (6) and associated descriptions for these two parameters) for all PDFs. The tendency appears to be for optical thickness to increase with increasing temperature and relative humidity. The ice water content basically depends on the amount of water vapor available for ice crystal formation in ice-supersaturated air. The available water vapor amount available is abundant under warm and humid conditions and generates large optical thicknesses consistent with model simulations [*Palikonda et al.*, 2005; *Kärcher et al.*, 2009; *Unterstrasser and Gierens*, 2010]. Many older contrails tend to become optically thinner (Figure 10c).

5. Interpretation Utilizing Theoretical Calculations

5.1. Computation Descriptions

[39] To interpret the observational results, the single-scattering properties of ice particles were simulated on the basis of the Lorenz-Mie theory for spherical ice particles and the Improved Geometrical Optics Method (IGOM) [*Yang and Liou*, 1996; *Bi et al.*, 2009] for randomly oriented nonspherical ice crystals. In the scattering calculations, we used a combination of ice crystal habits: spheres, droxtals, solid/hollow columns, plates, solid/hollow bullet rosettes, and aggregates. The geometrical representation of each ice crystal habit has been described by *Yang et al.* [2000, 2005]. Size-dependent particle geometry in terms of aspect ratio and hollowness has been accounted for columns, plates and bullet rosettes. Although the theoretical phase function typically exhibits halo features for pristine ice crystals larger than $\sim$40 μm, the halos have not commonly been observed in the atmosphere. The presence of surface roughness, irregular shapes, and air bubbles in ice particles are possible explanations for featureless phase functions [*Nousiainen and McFarquhar*, 2004; *Shcherbakov et al.*, 2006; *Yang et al.*, 2008; *Baran*, 2009; *Xie et al.*, 2009]. In this study, the particle surface roughness was assumed to obey the two-dimensional Gaussian distribution model expressed by a single parameter σ [*Yang et al.*, 2008], where $\sigma = 0$ for smooth particles. The new IGOM code was used by *Baum et al.* [2011] to compare theoretical backscattering

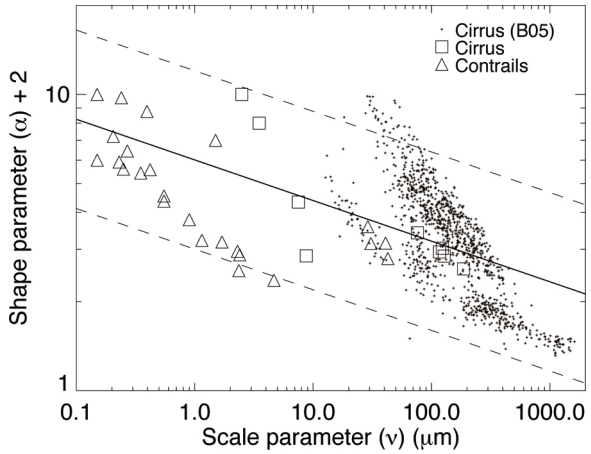

Figure 11. Relationship between the shape parameter (α) and the scale parameter (ν) of the particle size distribution represented by the Gamma distribution. Data obtained from in situ measurements presented by *Baum et al.* [2005] (denoted by B05) are shown by dots. Data computed from previous in situ measurements presented in the literature are shown by squares for cirrus clouds and triangles for contrails. The solid line denotes a least squares fit, and the dashed lines denote equations with twofold α + 2 smaller or larger values than the least squares fit.

properties with CALIOP observations for cirrus in which the results show better comparison by taking into account the surface roughness of ice crystals.

[40] In actual cirrus clouds (and contrails), various ice crystal habits and sizes coexist. Thus, the bulk scattering properties should be computed by accounting for both habit fraction and particle size distribution (PSD). An arbitrary bulk scattering property can be represented by introducing the following integral operator:

$$\{\hat{X}\}_{bulk} = \int_{D_{\min}}^{D_{\max}} n(D) \sum_j h_j(D)\hat{X}_j(D)dD, \tag{7}$$

where the arbitrary parameter D represents the particle size with a size range between $D_{\min}$ and $D_{\max}$. Equation (7) also includes the number density $n(D)$, a size-dependent habit fraction $h_j(D)$ for habit j, and the scattering property $\hat{X}_j(D)$ for a single particle. Using equation (7), the scattering efficiency Q_{sca} and the phase function P_{11} for an ice crystal habit mixture can be written as

$$Q_{sca} = \{\hat{A}_{sca}\}_{bulk}/\{\hat{A}_{geo}\}_{bulk}, \tag{8}$$

$$P_{11} = \{\hat{A}_{sca}\hat{P}_{11}\}_{bulk}/\{\hat{A}_{geo}\}_{bulk}, \tag{9}$$

where $\hat{A}_{sca}$ and $\hat{A}_{geo}$ are the particle scattering cross section and orientation-averaged geometrical projected area. The effective diameter D_{eff} is defined by [*Foot*, 1988; *Baum et al.*, 2005, and references therein]

$$D_{eff} = \frac{3}{2}\{\hat{V}\}_{bulk}/\{\hat{A}_{geo}\}_{bulk}, \tag{10}$$

where $\hat{V}$ is the volume of a single ice crystal. The lidar ratio S (sr) and the LDR are given by

$$S = \frac{4\pi}{\omega P_{11}(\pi)}, \tag{11}$$

$$\delta = \frac{P_{11}(\pi) - P_{22}(\pi)}{P_{11}(\pi) + P_{22}(\pi)}, \tag{12}$$

where ω is the single-scattering albedo and the symbol P denotes the scattering matrix elements. These parameters were computed at the 532 nm wavelength at which ω = 1. Thus, the lidar ratio is a function of $P_{11}(\pi)$ only.

[41] The PSD can be represented by the following function:

$$n(D) = N_0(D/\nu)^{\alpha-1}\exp(D/\nu), \tag{13}$$

for D ranging from $D_{\min}$ to $D_{\max}$. In equation (13), N_0 is a normalization factor, D is the maximum dimension, and α and ν are the shape and scale parameters. We used the values, $D_{\min}$ = 2 μm and $D_{\max}$ = 10000 μm. If $\alpha > 0$, $D_{\min} = 0$ and $D_{\max} = \infty$, equation (13) obeys the Gamma distribution.

[42] If the ice crystal shape is known, the two parameters, α and ν, can be estimated from any two parameters among the mean and effective sizes, average volume, and geometrical and extinction cross sections. In conjunction with this, we used estimates from the in situ measurements in contrails and cirrus clouds presented previously [*Gayet et al.*, 1996; *Petzold et al.*, 1997; *Goodman et al.*, 1998; *Schröder et al.*, 2000; *Febvre et al.*, 2009]. For simplicity of analysis, the ice crystal shapes were assumed to be exclusively spherical. Although the assumption can introduce errors in the parameter estimation, the present purpose was to investigate a rough relationship between α and ν. In many contrail cases, particularly young contrails, ice crystals were reported to have nearly spherical, quasi-spherical, or compact geometries with an aspect ratio close to 1. Our estimations appear to be reasonable for young contrails.

[43] Figure 11 shows the relationship between α and ν. The cirrus PSD data compiled by *Baum et al.* [2005] were plotted in addition to present contrails and cirrus estimates. Compared to those for cirrus clouds, contrails have a large α and a significantly smaller ν, which agrees with narrow PSDs observed when small particle sizes are dominant [*Petzold et al.*, 1997; *Poellot et al.*, 1999; *Schröder et al.*, 2000; *Schumann et al.*, 2011]. The α values generally decrease with increasing ν and broaden the PSD with increasing particle sizes. Large deviations were apparent between samples and no distinct differences were found between contrails and cirrus clouds. Therefore, a single least squares fit has been developed to include both contrails and cirrus:

$$\alpha + 2 = 6.01\nu^{-0.137}. \tag{14}$$

In determining the coefficients in equation (14), we used a tenfold larger weight for present contrails and cirrus estimates than that presented by *Baum et al.* [2005]. As shown in Figure 11, most data lay in the α + 2 range either twofold smaller or larger than the fitting curve. Equation (14) is useful because it represents PSDs analytically, and by changing the shape parameter, we can investigate the possible sensitivity

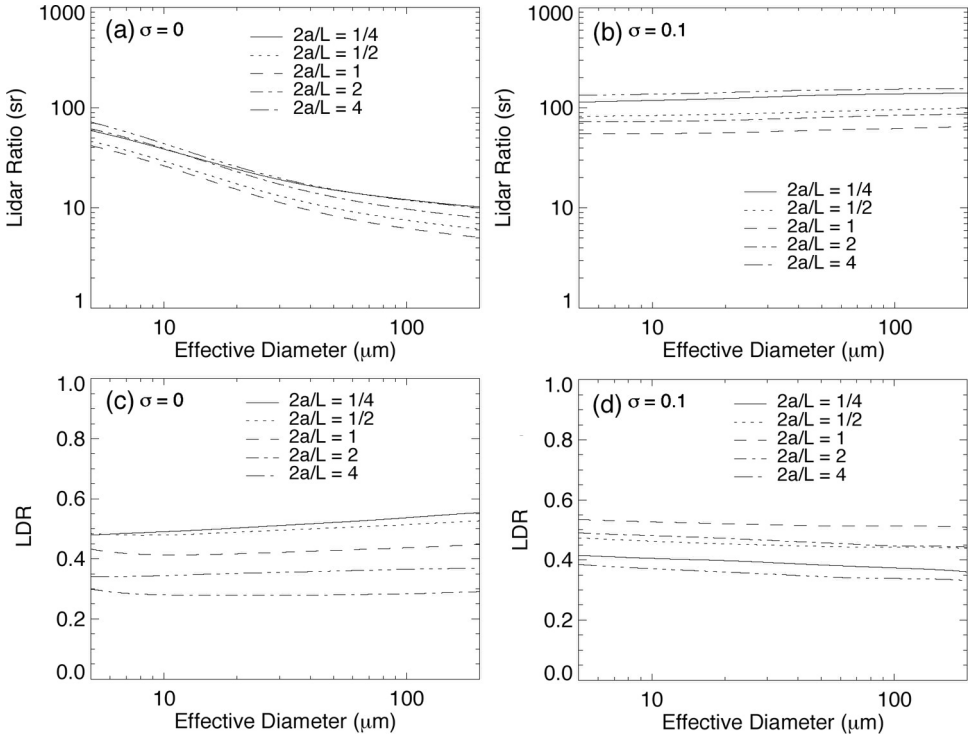

Figure 12. Derived from Improved Geometrical Optics Method (IGOM) calculations: (a and b) the theoretical lidar ratio and (c and d) LDR at a wavelength of 532 nm as functions of the effective particle diameter for hexagonal particle polydispersions with various aspect ratios ($2a/L$). Random particle orientation is assumed. Results are shown for smooth particles ($\sigma = 0$) (Figures 12a and 12c) and particles with moderate surface roughness ($\sigma = 0.1$) (Figures 12b and 12d).

between the optical properties and PSD width. Preliminary tests showed that a twofold change of $\alpha + 2$ results in only slight optical property differences when compared with a fixed D_{eff}. At a visible wavelength (532 nm), the maximum difference was 1% for the extinction efficiency and the asymmetry factor, 2% for LDR, and 15% for the lidar ratio. In the subsequent calculations, we used the relationship defined in equation (14).

5.2. Hexagonal Ice Crystals

[44] Figure 12 shows the lidar ratio and LDR as functions of the D_{eff} for hexagonal and polydisperse ice crystals with various aspect ratios ($2a/L$). For smooth ice crystals, the lidar ratio decreases with increasing D_{eff}. Compact ice crystals ($2a/L \sim 1$) exhibit the lowest lidar ratio. In the range of $D_{\text{eff}} = 10$–100 μm, the lidar ratio varies between 5 and 50 sr. The predicted LDR is sensitive to the aspect ratio but not to D_{eff}. For smooth particles ($\sigma = 0$), a monotonic variation of LDR with aspect ratio is shown. In this case, higher LDR values are predicted for greater aspect ratios. LDRs are 0.48–0.55 for columnar particles ($2a/L < 1$) and 0.28–0.37 for plate-like particles ($2a/L > 1$). *Noel et al.* [2002] interpreted the higher LDRs observed for colder particles as an indicator of higher aspect ratios. When ice crystals are moderately rough with $\sigma = 0.1$, compact hexagonal particles ($2a/L = 1$) exhibit the highest LDR, while aspect ratio deviations from unity result in smaller LDRs. This suggests a different interpretation that smaller particles are more compact, which may partly explain the higher LDR observed when this type of particles is dominant as noted previously. The particle surface roughness has a significant effect on backscattering properties. Supplemental tests showed that with low roughness (e.g., $\sigma = 0.001$), the lidar ratio was high (>50 sr) and not sensitive to D_{eff}, while the backscattering peak was smoothed in the phase function.

5.3. Habit Mixtures

[45] The dominant contrail ice habits likely depend on particle size. On the basis of several reports found in the literature, we tested three mixture models with size-dependent habit fractions, as illustrated in Figure 13. Habit fractions vary linearly with respect to log$D$ between anchor points at $D = 5$, 20, 100, 500, and 2000 μm. In situ measurements showed that the small particles ($D < 50$ μm) found in young contrails and aged contrail cores are either nearly spherical or compact particles [*Goodman et al.*, 1998; *Schröder et al.*, 2000; *Febvre et al.*, 2009]. In the present model, small particles are represented by droxtals [*Yang et al.*, 2005], which are compact faceted particles. In the contrail periphery, large particles, primarily columns with $D < 200$ μm and bullet rosettes with $D < \sim 300$ μm, were found by *Heymsfield et al.* [1998] and *Lawson et al.* [1998]. The moderate size range of $D = 20$–500 μm is the most important in the determination of optical properties of aged contrails. Thus, we used a mixture involving columns, plates, and bullet rosettes as the prime components denoted as mixture model 1. In some aged contrail cases, ice crystal shape has been reported as irregular. The measurements [*Gayet et al.*, 1996, 1998; *Febvre et al.*, 2009] taken in various ice clouds revealed that irregular ice crystals dominate in the

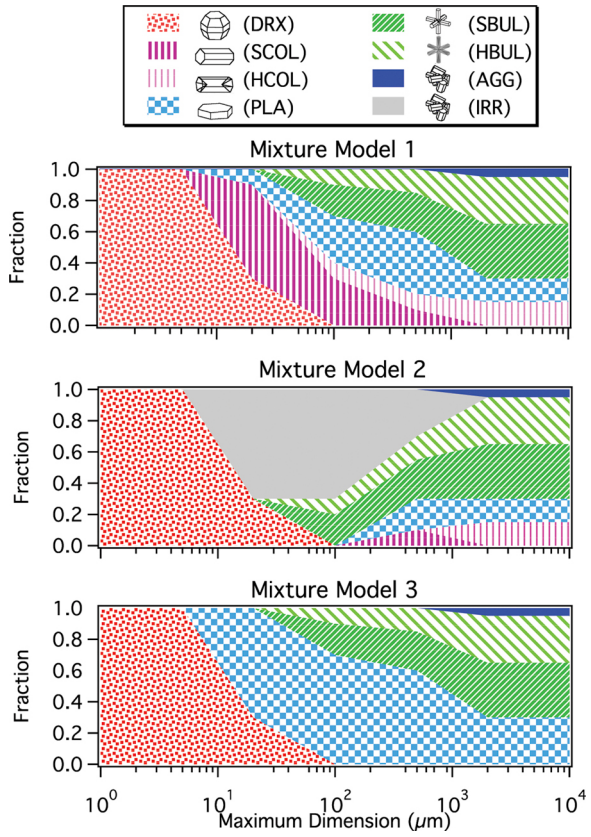

Figure 13. Ice crystal habit fractions, as functions of the maximum dimension, for habit mixture models 1–3. Considered ice crystal habits include droxtals (DRX), solid/hollow columns (SCOL/HCOL), plates (PLA), solid/hollow bullet rosettes (SBUL/HBUL), aggregates (AGG), and irregulars (IRR).

size range between 20 to 200 μm [*Korolev et al.*, 2000; *Heymsfield and McFarquhar*, 2002; *Whiteway et al.*, 2004; *Gallagher et al.*, 2005; *Baker and Lawson*, 2006; *Lawson et al.*, 2006]. The appropriate morphological representation of irregular ice crystals is not well known, however. In the present model, we used an aggregate of hexagonal ice crystals with moderate surface roughness (σ = 0.1) as a surrogate for an irregular ice crystal. The irregular ice crystal model does not produce halos and exhibits a smooth phase function with an asymmetry factor of 0.76, which is comparable to the quasi-spherical, irregular ice crystals found by *Nousiainen and McFarquhar* [2004], and a relatively high LDR of ~0.54. Thus, the habit mixture model 2 included a significant fraction of moderately sized, irregular ice crystals. For comparison purposes, mixture model 3 included several plate types instead of columns.

[46] Figure 14 shows the relationships between computed LDR and lidar ratio for each ice crystal habit and habit mixture model and a reasonable range determined from observations. The δ ranges are defined as the average plus/minus one standard deviation as obtained from our CALIOP contrail data analysis. We found only one published report of a contrail lidar ratio. *Langford et al.* [2005] observed contrails over Boulder, Colorado and obtained S = 13–40 sr for the majority of contrails. For optically thin cirrus (τ < 1) in cold air ($T < -40$°C), a reasonable range of S is from 10 to 50 sr, on the basis of previous studies [*Sassen and Comstock*, 2001; *Chen et al.*, 2002; *Immler and Schrems*, 2002; *Reichardt et al.*, 2002; *Immler et al.*, 2008]. This range generally agrees with the results reported by *Langford et al.* [2005]. Figure 14a shows a variety of δ and S pairs as a function of the ice crystal habit and the surface roughness. Spherical particles exhibit zero depolarization with S values from 15 to 20 sr. The CALIOP observations suggest that ice spheres are not dominant in the persistent contrails analyzed in this study. Except for spheres, only smooth plates have relatively low δ values (0.3–0.36). The other habits (droxtals, hollow columns, solid/hollow bullet rosettes, and column aggregates) with smooth surfaces exhibit higher δ values (0.4–0.57). In most cases, surface roughness does not significantly alter LDRs but results in higher lidar ratios. For most habits, the computed lidar ratios for rough particles are far over a reasonable range. As shown in Figure 14b, all of the three smooth-surfaced habit mixture models exhibit δ and S within reasonable ranges. Model 3 exhibits a lower value of δ than the other two, a result due to the dominance

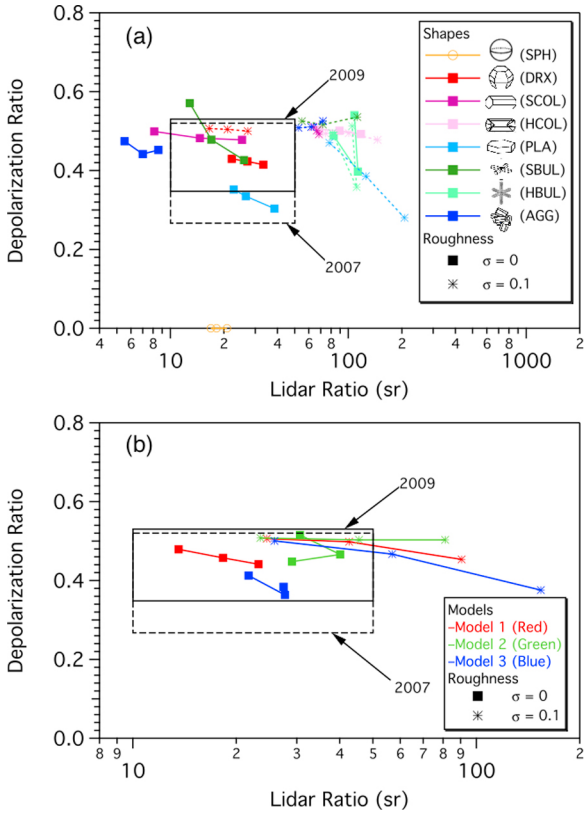

Figure 14. Theoretical relationships between LDR and lidar ratio for (a) ice particle habits and (b) habit mixture models. For each habit or habit mixture model, three points correspond to effective diameters of 10, 20, and 50 μm. A sphere habit is denoted by SPH, and other habit notations are the same as those in Figure 13. Superimposed rectangles denote ranges of LDR for contrails obtained from CALIOP data analysis in this study (average plus/minus one standard deviation) and a possible range of lidar ratio obtained in previous lidar measurements for contrail and optically thin natural cirrus cloud.

of plates. When surface roughness is present, the lidar ratio is too high for $D_{eff} > \sim 20$ μm, which suggests only a weak contribution of rough surface particles in detected contrails. Finally, it should be noted that observational studies of natural cirrus clouds indicate a general increase in the lidar ratio with increasing optical thickness [*Sassen and Comstock*, 2001; *Chen et al.*, 2002].

5.4. Discussion

[47] The CALIOP results suggest that the LDR tends to be high when ice crystal sizes are small, while individual ice crystal habits and the mixture models (Figures 12 and 14) show that LDR depends weakly on particle size. Contrails with small vertical extents yield very high δ values (>0.6) (Figure 8b), whereas the highest theoretical value of δ was approximately 0.57 (Figures 12 and 14) when faceted ice crystals were assumed in our calculations. The observed very high δ could be related to the dominance of very small (D_{eff} = 2–5 μm) quasi-spherical particles either present when the initial frozen droplets grow slowly or when ice crystals are evaporating in the subsaturated ambient air. *Mishchenko and Sassen* [1998] demonstrated that small quasi-spherical particles with a slight-to-moderate degree of asphericity could lead to large LDR.

[48] However, very high δ values were rather infrequent. Most detected contrails were considered to be older than ~2 min with high humidity (Figure 4c). Under such a condition, model simulations [*Kärcher et al.*, 2009; *Unterstrasser and Gierens*, 2010; *Unterstrasser and Solch*, 2010] and satellite and ground-based remote sensing results [*Duda et al.*, 1998; *Minnis et al.*, 1998; *Langford et al.*, 2005] suggest that D_{eff} is in a range of 10–90 μm. A typical value of D_{eff} = 20 μm appears to be a reasonable choice, although on average, a temperature- or age-dependent value may be more accurate. Assuming the D_{eff} in a range of 10–50 μm, any of the tested habit mixture models can explain the observed average LDRs such that it is not possible to select an optimal model a priori (Figure 14). The effects produced by different combination of irregular shape representations, surface roughness, and air bubbles in ice crystals could explain observed backscattering properties for which our current knowledge is limited [*Korolev et al.*, 2000; *Korolev and Isaac*, 2003; *Nousiainen and McFarquhar*, 2004; *Shcherbakov et al.*, 2006]. Indeed, more studies are needed in this area.

[49] The presence of horizontally oriented plates could provide a possible explanation for lower δ values for larger particle sizes. In the actual atmosphere, large plates may flutter with their asymmetry axes aligned nearly vertically. The flutter angle may also depend on the particle size and shape and is estimated to be in a range of 0.3°–2° [*Sassen*, 1991; *Reichardt et al.*, 2002]. Large plates with a small flutter angle can cause significantly strong backscattering due to specular reflection only when the lidar-pointing angle is small. Smaller plates with larger flutter angles may show relatively weak backscattering enhancement even for larger lidar-pointing angles. The lidar ratio and LDR are expected to be substantially reduced if a small fraction of the ice crystals are oriented horizontally. For example, *Sassen and Benson* [2001] and *Reichardt et al.* [2002] suggested the presence of 0.1–1% oriented ice particles was sufficient to lower the δ value from 0.4 to 0.3. Therefore, with increasing particle sizes, increasing the population fraction and/or decreasing the flutter angle of the oriented plates could explain the reduction in the LDR of scattering volume. Small particles, which are dominant in young contrails, contrail cores and at low temperatures, are expected to be randomly oriented. Their LDRs observed by off-nadir pointing are relatively high and generally agree with the theoretical prediction for habit mixtures. As shown in section 4, our observations indicate slight but nonnegligible influences by oriented plates, particularly in old contrails and cirrus clouds. With increasing particle sizes, the influence of specular reflection on backscattering and LDR could also increase. This may explain why the LDR is lower when larger particles are dominant in present results.

6. Conclusions

[50] Combined CALIOP and MODIS observations were used to derive statistics of the physical and optical properties of persistent contrails (or contrail cirrus), which were detected by a MODIS image analysis relying on the fact that their artificial shapes are easily distinguished from natural cirrus. Collocated CALIOP data were analyzed to derive geometrical and optical properties of approximately 3400 detected contrails over a region including North America, the North Atlantic Ocean, Greenland, and Europe. Lidar-derived optical properties were compared between contrails and the neighboring cirrus. Highlights of this investigation are summarized as follows:

[51] 1. The mean altitude of detected contrail tops is 10.9 km and decreases with increasing latitude. The mean temperature at contrail top is about −55°C, and the majority of detected contrails are found at temperatures below −40°C, implying that ice crystal nucleation by homogeneous freezing of liquid droplets may be the primary mechanism for contrail formation. On the basis of the meteorological model analysis, the average relative humidity with respect to ice (RH_{ice}) is about 125% at the midlevel, and 65% of detected contrails are found in moderately supersaturated air (100% < RH_{ice} < 150%).

[52] 2. Target contrails were very large with mean width, thickness, and length as large as 6, 0.8, and 264 km, respectively, because we included numerous aged contrails in the analysis. The contrail width is approximately proportional to the square of the thickness. Geometrically thick contrails can grow in humid environments.

[53] 3. It is suggested that during aging, contrail optical properties change to become closer to those of neighboring cirrus, although our classification by age could be ambiguous. The LDR is high in young contrails (age < ~13 min) and in contrail cores, but is low along the peripheries. Furthermore, the LDR for detected contrails weakly depends on lidar pointing angle when compared to cirrus clouds. This weak dependence suggests that contrails are mainly composed of small, randomly oriented ice crystals containing a few (but nonnegligible on the basis of vertically pointing lidar observations) horizontally oriented plates.

[54] 4. The observed LDR average and variation are generally consistent with theoretical simulations based on a mixture of nonspherical ice crystals with random orientations. In particular, except for very fresh contrails in the vortex phase (<2 min), young contrails are characterized by a high concentration of small particles that are randomly

oriented and exhibit relatively high LDRs. Small particles can be represented by compact geometries or nearly spherical particles.

[55] 5. Relatively thin contrails occasionally exhibit strong depolarization ($\delta > 0.6$) that cannot be explained by a number of faceted ice crystals assumed in this study. A possible explanation may be that very small ($D_{\text{eff}} = 2$–5 μm), nearly spherical particles dominate when particles slowly grow/evaporate in ambient air with a relative humidity close to 100%. Previous theoretical simulations [*Mishchenko and Sassen*, 1998] suggested that small quasi-spherical ice particles with a slight-to-moderate degree of asphericity might be responsible for strong contrail depolarization.

[56] 6. Most detected contrails are optically thin. The mean (median) optical thickness of detected contrails is about 0.19 (0.14) with a large variability, according to off-nadir observations. About 34% of detected contrails have $\tau < 0.1$. Thick contrails with $\tau > 0.5$ account for only 5% of off-nadir and 10% of quasi-nadir observations, respectively. A detection limit of optically very thin (subvisual) contrails could have an impact on the statistics of all persistent contrails and contrail cirri that were not detected in the present methodology.

[57] 7. Optically thicker contrails do exist and tend to occur in warmer and more humid ambient air. It is also suggested that aging generally tends to decrease the optical thickness.

[58] As shown in section 5, the lidar ratio is very sensitive to ice particle size, shape, and surface roughness. The cirrus lidar ratio dependence on optical thickness and temperature [*Sassen and Comstock*, 2001; *Chen et al.*, 2002] reveals a linkage between microphysical properties and meteorological conditions. Possible variation in the lidar ratio and the multiple scattering effects could be the major causes of optical thickness uncertainty, which could be effectively reduced by an improved retrieval algorithm or new lidar techniques. At present, our understanding of backscattering properties for contrails and contrail cirrus is still limited. The present study demonstrated that measurements of the linear depolarization and lidar ratios alone are not sufficient to uniquely determine an ice crystal mode for these clouds: further studies are required using remote sensing techniques and in situ measurements. Possible improvements could also be expected by application of the passive remote sensing techniques to retrieve ice particle effective diameters and optical thicknesses [e.g., *Betancor-Gothe and Grassl*, 1993; *Duda et al.*, 1998].

[59] **Acknowledgments.** This work was supported by the Aviation Climate Change Research Initiative (ACCRI) sponsored by the Federal Aviation Administration (FAA) under contracts DTRT57-10-C-10016 and DTRT57-10-X-70020. The authors thank Rangasayi Halthore and S. Daniel Jacob from the FAA for overseeing the project progress and for guidance and encouragement. The authors are grateful to Ulrich Schumann, Bernd Kärcher, and an anonymous reviewer for constructive comments and suggestions. The CALIPSO data were obtained from the NASA Langley Research Center Atmospheric Science Data Center. The MODIS data were obtained from NASA/GSFC, MODIS Rapid Response System, and the Level 1 and Atmosphere Archive and Distribution System (LAADS).

References

Atlas, D., Z. Wang, and D. P. Duda (2006), Contrails to cirrus: Morphology, microphysics, and radiative properties, *J. Appl. Meteorol. Climatol.*, *45*(1), 5–19, doi:10.1175/JAM2325.1.

Baker, B. A., and R. P. Lawson (2006), In situ observations of the microphysical properties of wave, cirrus, and anvil clouds. Part I: Wave clouds, *J. Atmos. Sci.*, *63*(12), 3160–3185, doi:10.1175/JAS3802.1.

Baran, A. J. (2009), A review of the light scattering properties of cirrus, *J. Quant. Spectrosc. Radiat. Transfer*, *110*(14–16), 1239–1260, doi:10.1016/j.jqsrt.2009.02.026.

Baum, B. A., A. J. Heymsfield, P. Yang, and S. T. Bedka (2005), Bulk scattering properties for the remote sensing of ice clouds. Part I: Microphysical data and models, *J. Appl. Meteorol.*, *44*(12), 1885–1895, doi:10.1175/JAM2308.1.

Baum, B. A., P. Yang, A. J. Heymsfield, C. G. Schmitt, Y. Xie, A. Bansemer, Y.-X. Hu, and Z. Zhang (2011), Improvements in shortwave bulk scattering and absorption models for the remote sensing of ice clouds, *J. Appl. Meteorol. Climatol.*, *50*(5), 1037–1056, doi:10.1175/2010JAMC2608.1.

Baumgardner, D., and B. E. Gandrud (1998), A comparison of the microphysical and optical properties of particles in an aircraft contrail and mountain wave cloud, *Geophys. Res. Lett.*, *25*(8), 1129–1132, doi:10.1029/98GL00035.

Betancor-Gothe, M., and H. Grassl (1993), Satellite remote-sensing of the optical depth and mean crystal size of thin cirrus and contrails, *Theor. Appl. Climatol.*, *48*(2–3), 101–113, doi:10.1007/BF00864917.

Bi, L., P. Yang, G. W. Kattawar, B. A. Baum, Y. X. Hu, D. M. Winker, R. S. Brock, and J. Q. Lu (2009), Simulation of the color ratio associated with the backscattering of radiation by ice crystals at 0.532 and 1.064 μm wavelengths, *J. Geophys. Res.*, *114*, D00H08, doi:10.1029/2009JD011759.

Brasseur, G. P., and M. Gupta (2010), Impact of aviation on climate, *Bull. Am. Meteorol. Soc.*, *91*(4), 461–463, doi:10.1175/2009BAMS2850.1.

Burkhardt, U., and B. Kärcher (2011), Global radiative forcing from contrail cirrus, *Nat. Clim. Change*, *1*, 54–58, doi:10.1038/nclimate1068.

Chen, W. N., C. W. Chiang, and J. B. Nee (2002), Lidar ratio and LDR for cirrus clouds, *Appl. Opt.*, *41*(30), 6470–6476, doi:10.1364/AO.41.006470.

Cho, H. M., P. Yang, G. W. Kattawar, S. L. Nasiri, Y. X. Hu, P. Minnis, C. Trepte, and D. Winker (2008), LDR and attenuated backscatter for nine cloud types: Analyses based on collocated CALIPSO lidar and MODIS measurements, *Opt. Express*, *16*(6), 3931–3948, doi:10.1364/OE.16.003931.

Del Guasta, M., and K. Niranjan (2001), Observation of low-depolarization contrails at Florence (Italy) using a 532–1064 nm polarization LIDAR, *Geophys. Res. Lett.*, *28*(21), 4067–4070, doi:10.1029/2001GL013635.

Duda, D. P., J. D. Spinhirne, and V. D. Hart (1998), Retrieval of contrail microphysical properties during SUCCESS by the split-window method, *Geophys. Res. Lett.*, *25*(8), 1149–1152, doi:10.1029/97GL03159.

Febvre, G., J. F. Gayet, A. Minikin, H. Schlager, V. Shcherbakov, O. Jourdan, R. Busen, M. Fiebig, B. Kärcher, and U. Schumann (2009), On optical and microphysical characteristics of contrails and cirrus, *J. Geophys. Res.*, *114*, D02204, doi:10.1029/2008JD010184.

Foot, J. S. (1988), Some observations of the optical properties of clouds. II: Cirrus, *Q. J. R. Meteorol. Soc.*, *114*(479), 145–164, doi:10.1002/qj.49711447908.

Freudenthaler, V., F. Homburg, and H. Jäger (1995), Contrail observations by ground-based scanning lidar: Cross-sectional growth, *Geophys. Res. Lett.*, *22*(24), 3501–3504, doi:10.1029/95GL03549.

Freudenthaler, V., F. Homburg, and H. Jäger (1996), Optical parameters of contrails from lidar measurements: Linear depolarization, *Geophys. Res. Lett.*, *23*(25), 3715–3718, doi:10.1029/96GL03646.

Gallagher, M. W., P. J. Connolly, J. Whiteway, D. Figueras-Nieto, M. Flynn, T. W. Choularton, K. N. Bower, C. Cook, R. Busen, and J. Hacker (2005), An overview of the microphysical structure of cirrus clouds observed during EMERALD-1, *Q. J. R. Meteorol. Soc.*, *131*(607), 1143–1169, doi:10.1256/qj.03.138.

Gayet, J. F., G. Febvre, G. Brogniez, H. Chepfer, W. Renger, and P. Wendling (1996), Microphysical and optical properties of cirrus and contrails: Cloud field study on 13 October 1989, *J. Atmos. Sci.*, *53*(1), 126–138, doi:10.1175/1520-0469(1996)053<0126:MAOPOC>2.0.CO;2.

Gayet, J. F., F. Auriol, S. Oshchepkov, F. Schröder, C. Duroure, G. Febvre, J. F. Fournol, O. Crépel, P. Personne, and D. Daugereon (1998), In situ measurements of the scattering phase function of stratocumulus, contrails and cirrus, *Geophys. Res. Lett.*, *25*(7), 971–974, doi:10.1029/98GL00541.

Goodman, J., R. F. Pueschel, E. J. Jensen, S. Verma, G. V. Ferry, S. D. Howard, S. A. Kinne, and D. Baumgardner (1998), Shape and size of contrails ice particles, *Geophys. Res. Lett.*, *25*(9), 1327–1330, doi:10.1029/97GL03091.

Heymsfield, A., and G. M. McFarquhar (2002), Mid latitude and tropical cirrus microphysical properties, in *Cirrus*, edited by D. K. Lynch et al., pp. 78–101, Oxford Univ. Press, New York.

Heymsfield, A. J., R. P. Lawson, and G. W. Sachse (1998), Growth of ice crystals in a precipitating contrail, *Geophys. Res. Lett.*, *25*(9), 1335–1338, doi:10.1029/98GL00189.

Heymsfield, A., D. Baumgardner, P. DeMott, P. Forster, K. Gierens, and B. Kärcher (2010), Contrail microphysics, *Bull. Am. Meteorol. Soc.*, *91*(4), 465–472, doi:10.1175/2009BAMS2839.1.

Hu, Y. X., et al. (2007), The depolarization-attenuated backscatter relation: CALIPSO lidar measurements vs. theory, *Opt. Express*, *15*(9), 5327–5332, doi:10.1364/OE.15.005327.

Immler, F., and O. Schrems (2002), LIDAR measurements of cirrus clouds in the northern and southern midlatitudes during INCA (55°N, 53°S): A comparative study, *Geophys. Res. Lett.*, *29*(16), 1809, doi:10.1029/2002GL015077.

Immler, F., R. Treffeisen, D. Engelbart, K. Krüger, and O. Schrems (2008), Cirrus, contrails, and ice supersaturated regions in high pressure systems at northern midlatitudes, *Atmos. Chem. Phys.*, *8*(6), 1689–1699, doi:10.5194/acp-8-1689-2008.

Jensen, E. J., A. S. Ackerman, D. E. Stevens, O. B. Toon, and P. Minnis (1998), Spreading and growth of contrails in a sheared environment, *J. Geophys. Res.*, *103*(D24), 31,557–31,567, doi:10.1029/98JD02594.

Kärcher, B., U. Burkhardt, S. Unterstrasser, and P. Minnis (2009), Factors controlling contrail cirrus optical depth, *Atmos. Chem. Phys.*, *9*(16), 6229–6254, doi:10.5194/acp-9-6229-2009.

Kärcher, B., U. Burkhardt, M. Ponater, and C. Frömming (2010), Importance of representing optical depth variability for estimates of global line-shaped contrail radiative forcing, *Proc. Natl. Acad. Sci. U. S. A.*, *107*(45), 19,181–19,184, doi:10.1073/pnas.1005555107.

Knollenberg, R. G. (1972), Measurements of growth of ice budget in a persisting contrail, *J. Atmos. Sci.*, *29*(7), 1367–1374, doi:10.1175/1520-0469(1972)029<1367:MOTGOT>2.0.CO;2.

Korolev, A., and G. Isaac (2003), Roundness and aspect ratio of particles in ice clouds, *J. Atmos. Sci.*, *60*(15), 1795–1808, doi:10.1175/1520-0469(2003)060<1795:RAAROP>2.0.CO;2.

Korolev, A., G. A. Isaac, and J. Hallett (2000), Ice particle habits in stratiform clouds, *Q. J. R. Meteorol. Soc.*, *126*(569), 2873–2902, doi:10.1002/qj.49712656913.

Langford, A. O., R. W. Portmann, J. S. Daniel, H. L. Miller, C. S. Eubank, S. Solomon, and E. G. Dutton (2005), Retrieval of ice crystal effective diameters from ground-based near-infrared spectra of optically thin cirrus, *J. Geophys. Res.*, *110*, D22201, doi:10.1029/2005JD005761.

Lawson, R. P., A. J. Heymsfield, S. M. Aulenbach, and T. L. Jensen (1998), Shapes, sizes and light scattering properties of ice crystals in cirrus and a persistent contrail during SUCCESS, *Geophys. Res. Lett.*, *25*(9), 1331–1334, doi:10.1029/98GL00241.

Lawson, R. P., B. Baker, B. Pilson, and Q. X. Mo (2006), In situ observations of the microphysical properties of wave, cirrus, and anvil clouds. Part II: Cirrus clouds, *J. Atmos. Sci.*, *63*(12), 3186–3203, doi:10.1175/JAS3803.1.

Lee, D. S., D. W. Fahey, P. M. Forster, P. J. Newton, R. C. N. Wit, L. L. Lim, B. Owen, and R. Sausen (2009), Aviation and global climate change in the 21st century, *Atmos. Environ.*, *43*(22–23), 3520–3537, doi:10.1016/j.atmosenv.2009.04.024.

Marquart, S., M. Ponater, F. Mager, and R. Sausen (2003), Future development of contrail cover, optical depth, and radiative forcing: Impacts of increasing air traffic and climate change, *J. Clim.*, *16*(17), 2890–2904, doi:10.1175/1520-0442(2003)016<2890:FDOCCO>2.0.CO;2.

Meerkötter, R., U. Schumann, D. R. Doelling, P. Minnis, T. Nakajima, and Y. Tsushima (1999), Radiative forcing by contrails, *Ann. Geophys.*, *17*(8), 1080–1094, doi:10.1007/s00585-999-1080-7.

Meyer, R., H. Mannstein, R. Meerkötter, U. Schumann, and P. Wendling (2002), Regional radiative forcing by line-shaped contrails derived from satellite data, *J. Geophys. Res.*, *107*(D10), 4104, doi:10.1029/2001JD000426.

Minnis, P., D. F. Young, D. P. Garber, L. Nguyen, W. L. Smith, and R. Palikonda (1998), Transformation of contrails into cirrus during SUCCESS, *Geophys. Res. Lett.*, *25*(8), 1157–1160, doi:10.1029/97GL03314.

Minnis, P., J. K. Ayers, M. L. Nordeen, and S. P. Weaver (2003), Contrail frequency over the United States from surface observations, *J. Clim.*, *16*(21), 3447–3462, doi:10.1175/1520-0442(2003)016<3447:CFOTUS>2.0.CO;2.

Minnis, P., J. K. Ayers, R. Palikonda, and D. Phan (2004), Contrails, cirrus trends, and climate, *J. Clim.*, *17*(8), 1671–1685, doi:10.1175/1520-0442(2004)017<1671:CCTAC>2.0.CO;2.

Minnis, P., R. Palikonda, B. J. Walter, J. K. Ayers, and H. Mannstein (2005), Contrail properties over the eastern North Pacific from AVHRR data, *Meteorol. Z.*, *14*(4), 515–523, doi:10.1127/0941-2948/2005/0056.

Mishchenko, M. I., and K. Sassen (1998), Depolarization of lidar returns by small ice crystals: An application to contrails, *Geophys. Res. Lett.*, *25*(3), 309–312, doi:10.1029/97GL03764.

Noel, V., H. Chepfer, G. Ledanois, A. Delaval, and P. H. Flamant (2002), Classification of particle effective shape ratios in cirrus clouds based on the lidar depolarization ratio, *Appl. Opt.*, *41*, 4245–4257, doi:10.1364/AO.41.004245.

Nousiainen, T., and G. M. McFarquhar (2004), Light scattering by quasi-spherical ice crystals, *J. Atmos. Sci.*, *61*(18), 2229–2248, doi:10.1175/1520-0469(2004)061<2229:LSBQIC>2.0.CO;2.

Palikonda, R., P. Minnis, D. P. Duda, and H. Mannstein (2005), Contrail coverage derived from 2001 AVHRR data over the continental United States of America and surrounding areas, *Meteorol. Z.*, *14*(4), 525–536, doi:10.1127/0941-2948/2005/0051.

Penner, J. E., D. H. Lister, D. J. Griggs, D. J. Dokken, and M. McFarland (Eds.) (1999), *Aviation and the Global Atmosphere*, 373 pp., Cambridge Univ. Press, New York.

Petzold, A., et al. (1997), Near-field measurements on contrail properties from fuels with different sulfur content, *J. Geophys. Res.*, *102*(D25), 29,867–29,880, doi:10.1029/97JD02209.

Poellot, M. R., W. P. Arnott, and J. Hallett (1999), In situ observations of contrail microphysics and implications for their radiative impact, *J. Geophys. Res.*, *104*(D10), 12,077–12,084, doi:10.1029/1999JD900109.

Ponater, M., S. Brinkop, R. Sausen, and U. Schumann (1996), Simulating the global atmospheric response to aircraft water vapour emissions and contrails: A first approach using a GCM, *Ann. Geophys.*, *14*(9), 941–960, doi:10.1007/s00585-996-0941-6.

Reichardt, J., S. Reichardt, M. Hess, and T. J. McGee (2002), Correlations among the optical properties of cirrus-cloud particles: Microphysical interpretation, *J. Geophys. Res.*, *107*(D21), 4562, doi:10.1029/2002JD002589.

Reichardt, S., and J. Reichardt (2003), Effect of multiple scattering on depolarization measurements with spaceborne lidars, *Appl. Opt.*, *42*(18), 3620–3633, doi:10.1364/AO.42.003620.

Sassen, K. (1979), Iridescence in an aircraft contrail, *J. Opt. Soc. Am.*, *69*(8), 1080–1083, doi:10.1364/JOSA.69.001080.

Sassen, K. (1991), The polarization lidar technique for cloud research: A review and current assessment, *Bull. Am. Meteorol. Soc.*, *72*(12), 1848–1866, doi:10.1175/1520-0477(1991)072<1848:TPLTFC>2.0.CO;2.

Sassen, K. (1997), Contrail-cirrus and their potential for regional climate change, *Bull. Am. Meteorol. Soc.*, *78*(9), 1885–1903, doi:10.1175/1520-0477(1997)078<1885:CCATPF>2.0.CO;2.

Sassen, K., and S. Benson (2001), A midlatitude cirrus cloud climatology from the facility for atmospheric remote sensing. Part II: Microphysical properties derived from lidar depolarization, *J. Atmos. Sci.*, *58*(15), 2103–2112, doi:10.1175/1520-0469(2001)058<2103:AMCCCF>2.0.CO;2.

Sassen, K., and J. M. Comstock (2001), A midlatitude cirrus cloud climatology from the facility for atmospheric remote sensing. Part III: Radiative properties, *J. Atmos. Sci.*, *58*(15), 2113–2127, doi:10.1175/1520-0469(2001)058<2113:AMCCCF>2.0.CO;2.

Sassen, K., and C. Y. Hsueh (1998), Contrail properties derived from high-resolution polarization lidar studies during SUCCESS, *Geophys. Res. Lett.*, *25*(8), 1165–1168, doi:10.1029/97GL03503.

Sassen, K., and J. Zhu (2009), A global survey of CALIPSO linear dipolarization ratios in ice clouds: Initial findings, *J. Geophys. Res.*, *114*, D00H07, doi:10.1029/2009JD012279.

Schröder, F., B. Kärcher, C. Duroure, J. Strom, A. Petzold, J. F. Gayet, B. Strauss, P. Wendling, and S. Borrmann (2000), On the transition of contrails into cirrus clouds, *J. Atmos. Sci.*, *57*(4), 464–480, doi:10.1175/1520-0469(2000)057<0464:OTTOCI>2.0.CO;2.

Schumann, U. (2002), Contrail cirrus, in *Cirrus*, edited by D. K. Lynch et al., pp. 231–255, Oxford Univ. Press, New York.

Schumann, U., B. Mayer, K. Gierens, S. Unterstrasser, P. Jessberger, A. Petzold, C. Voigt, and J. F. Gayet (2011), Effective radius of ice particles in cirrus and contrails, *J. Atmos. Sci.*, *68*(2), 300–321, doi:10.1175/2010JAS3562.1.

Shcherbakov, V., J. F. Gayet, B. Baker, and P. Lawson (2006), Light scattering by single natural ice crystals, *J. Atmos. Sci.*, *63*(5), 1513–1525, doi:10.1175/JAS3690.1.

Sussmann, R. (1997), Optical properties of contrail-induced cirrus: Discussion of unusual halo phenomena, *Appl. Opt.*, *36*(18), 4195–4201.

Sussmann, R., and K. M. Gierens (1999), Lidar and numerical studies on the different evolution of vortex pair and secondary wake in young contrails, *J. Geophys. Res.*, *104*(D2), 2131–2142, doi:10.1029/1998JD200034.

Sussmann, R., and K. M. Gierens (2001), Differences in early contrail evolution of two-engine versus four-engine aircraft: Lidar measurements and numerical simulations, *J. Geophys. Res.*, *106*(D5), 4899–4911, doi:10.1029/2000JD900533.

Unterstrasser, S., and K. Gierens (2010), Numerical simulations of contrail-to-cirrus transition. Part I: An extensive parametric study, *Atmos. Chem. Phys.*, *10*(4), 2017–2036, doi:10.5194/acp-10-2017-2010.

Unterstrasser, S., and I. Solch (2010), Study of contrail microphysics in the vortex phase with a Lagrangian particle tracking model, *Atmos. Chem. Phys.*, *10*(20), 10,003–10,015, doi:10.5194/acp-10-10003-2010.

Voigt, C., U. Schumann, P. Jessberger, T. Jurkat, A. Petzold, J.-F. Gayet, M. Krämer, T. Thornberry, and D. W. Fahey (2011), Extinction and optical depth of contrails, *Geophys. Res. Lett.*, *38*, L11806, doi:10.1029/2011GL047189.

Whiteway, J., et al. (2004), Anatomy of cirrus clouds: Results from the Emerald airborne campaigns, *Geophys. Res. Lett.*, *31*, L24102, doi:10.1029/2004GL021201.

Xie, Y., P. Yang, G. W. Kattawar, P. Minnis, and Y. X. Hu (2009), Effect of the inhomogeneity of ice crystals on retrieving ice cloud optical thickness and effective particle size, *J. Geophys. Res.*, *114*, D11203, doi:10.1029/2008JD011216.

Yang, P., and K. N. Liou (1996), Geometric-optics-integral-equation method for light scattering by nonspherical ice crystals, *Appl. Opt.*, *35*(33), 6568–6584, doi:10.1364/AO.35.006568.

Yang, P., K. N. Liou, K. Wyser, and D. Mitchell (2000), Parameterization of the scattering and absorption properties of individual ice crystals, *J. Geophys. Res.*, *105*(D4), 4699–4718, doi:10.1029/1999JD900755.

Yang, P., H. L. Wei, H. L. Huang, B. A. Baum, Y. X. Hu, G. W. Kattawar, M. I. Mishchenko, and Q. Fu (2005), Scattering and absorption property database for nonspherical ice particles in the near- through far-infrared spectral region, *Appl. Opt.*, *44*(26), 5512–5523, doi:10.1364/AO.44.005512.

Yang, P., G. Hong, G. W. Kattawar, P. Minnis, and Y. X. Hu (2008), Uncertainties associated with the surface texture of ice particles in satellite-based retrieval of cirrus clouds. Part II: Effect of particle surface roughness on retrieved cloud optical thickness and effective particle size, *IEEE Trans. Geosci. Remote Sens.*, *46*(7), 1948–1957, doi:10.1109/TGRS.2008.916472.

Yang, P., G. Hong, A. E. Dessler, S. S. C. Ou, K. N. Liou, P. Minnis, and Harshvardhan (2010), Contrails and induced cirrus optics and radiation, *Bull. Am. Meteorol. Soc.*, *91*(4), 473–478, doi:10.1175/2009BAMS2837.1.

You, Y., G. W. Kattawar, P. Yang, Y. X. Hu, and B. A. Baum (2006), Sensitivity of depolarized lidar signals to cloud and aerosol particle properties, *J. Quant. Spectrosc. Radiat. Transfer*, *100*(1–3), 470–482, doi:10.1016/j.jqsrt.2005.11.058.

H. Iwabuchi and P. Yang, Department of Atmospheric Sciences, Texas A&M University, College Station, TX 77843, USA. (pyang@tamu.edu)

K. N. Liou, Joint Institute for Regional Earth System Science and Engineering, University of California, Los Angeles, CA 90095, USA.

P. Minnis, Science Directorate, NASA Langley Research Center, Hampton, VA 23682, USA.